Illuminating Excited-State Intramolecular Proton Transfer of A Fungi-Derived Red Pigment for Sustainable Functional Materials

Taylor D. Krueger,[a,§] Janak Solaris,[a,§] Longteng Tang,[a] Liangdong Zhu,[a] Carter Webber,[b] Ray C. Van Court,[c] Seri C. Robinson,[c] Oksana Ostroverkhova,[b] and Chong Fang*[,a]

[a] Department of Chemistry, Oregon State University, 153 Gilbert Hall, Corvallis, Oregon 97331, United States

[b] Department of Physics, Oregon State University, 301 Weniger Hall, Corvallis, Oregon 97331, United States

[c] Department of Wood Science and Engineering, Oregon State University, 119 Richardson Hall, Corvallis, Oregon 97331, United States

[§] These authors (T.D.K. and J.S.) contributed equally to this work.

* Corresponding Author: Chong.Fang@oregonstate.edu

Abstract. Proton transfer is an important player that contributes to functional properties of light-sensitive organic molecules from photostability to energy transfer. For an organic pigment secreted by the wood-spalting fungus *Scytalidium cuboideum*, little is known about Draconin Red despite its discovery decades earlier. With steady-state and time-resolved spectroscopic techniques as well as quantum calculations, two tautomers of Draconin Red with different orientations of hydroxy groups were found to comprise most of the equilibrium population. These tautomers may underlie major species in fluorescent and nonfluorescent needle-like crystals, the former showing waveguide properties. Femtosecond transient absorption measurements revealed a dynamic equilibrium due to excited-state intramolecular proton transfer (ESIPT) between the two tautomers on faster (<120 fs) and slower (~750 fs) timescales, supplemented by computationally scanning two nonequivalent ESIPT coordinates. Ground and excited-state femtosecond stimulated Raman spectroscopy (FSRS) confirmed the presence of both tautomers in solution with key frequency shifts of vibrational marker bands upon photoexcitation, tracking an initial ultrafast unidirectional tautomerization. We envision rational design of the highly symmetric red pigment by incorporation of electron donating and/or withdrawing groups to elevate the electronic and photonic performance of this naturally derived small molecule going from solution to solid state.

1. INTRODUCTION

As global energy demand increases, critical eyes have been directed toward the methods in which energy is harvested, stored, and utilized.[1,2] To meet this demand sustainably, novel methods of energy harvesting and transfer must be developed with a focus on optimizing efficiency, productivity, and reliability.[3,4] One field precipitated by this paradigm shift is that of organic electronic materials which boast low costs, attachment to flexible substrates, highly scalable solvent-based processing, and versatility through the informed design. While alternative and sustainable routes are progressing, existing organic electronics are subject to relatively low resilience to environmental stressors compared to their inorganic counterparts.[5,6]

Most promising about the development of durable organic electronics is the ubiquity of photosynthetic biological systems reliant on the capture, transport, and storage of light energy.[7-9] Natural photosynthetic systems provide the framework for the utilization of organic chromophores to absorb light across a broad wavelength range, promoting the chromophore into an excited state and separating non-equilibrium charges within the system. These complexes often utilize a series of protein-locked chromophores known as an antenna system to transport the absorbed energy as an exciton, where it can be converted into a usable form.[5,10-12] Among contributors to the relatively high efficiency of energy transfer in antenna complexes, coherent quantum beats have been observed in several light-harvesting systems, potentially aiding the energy transfer process.[13-15] Such beats retain coherence long enough to span the time required for the preparatory steps of energy transfer, increasing efficiency of the system beyond that predicted by incoherent light emission and re-absorption.[13,16-18] The superposition of vibrational and electronic energy levels forms vibronic energy states in which vibrational modes may facilitate electronic energy transfer, particularly for coherently excited vibrational modes with large displacements (large Huang-Rhys factors) that can be observed by femtosecond (fs) laser spectroscopy.[7,18] Quantum coherence could play an active role during energy transfer in photosynthetic systems, and allow the strongly coupled chromophores to act more as a single absorbing system, thus broadening and intensifying the absorption bands of the coupled system beyond individual capability of each chromophore.

Beyond a major electronic perspective, proton transfer is integral in various organic and biological systems and protects many chromophores by providing an efficient nondestructive pathway for energy dissipation after photoexcitation, which makes the excited-state proton transfer (ESPT) process to solvent or an adjacent proton acceptor (sensitizer) an active area of research.[19-30] In particular, when the proton donor and acceptor are within the same molecule at close proximity (e.g., between hydroxy and carbonyl/-nitrogen heterocyclic moieties), excited-state intramolecular proton transfer (ESIPT) can be a photoprotection mechanism for organic dyes by providing a relaxation pathway via tautomerization.[31-35] The ESIPT behavior in solution indicates that a molecule may facilitate charge transfer (CT) with a concomitant or separate path for proton transfer in solid-state materials.[35-37] The practical applications of ESIPT dyes are legion, ranging from use as laser dyes and bioimaging probes to quantum logic gates.[38,39]

Several well-characterized ESIPT dyes, such as 2-(2-hydroxyphenyl)benzothiazole and 2-(2-hydroxyphenyl)benzoxazole absorb outside the visible range, limiting their application for visible light processes. Many more thoroughly studied ESIPT dyes have been derived from nitrogen-ring systems such as naphthylamides, indoles, or pyrazoles, which commonly exhibit reduced ESIPT capability due to the less acidic nature of amine protons compared to hydroxy protons.[40-42] Investigations into the hydroxy-based ESIPT systems such as alizarin have been prolific,[43-47] but studies of ultrafast ESIPT processes have only been made possible using ultrafast lasers on an ESIPT reaction as fast as 13 fs in 10-hydroxybenzo[*h*]quinoline.[48]

Notably, the compound 2,7-dimethoxynaphthazarin (i.e., 5,8-dihydroxy-2,7-dimethoxy-1,4-naphthoquinone), or Draconin Red, is a red pigment produced by the spalting wood fungus *Scytalidium cuboideum*. Such spalting fungi have been found still intact in stained wood used in intarsia artwork dating back to the 15th century, demonstrating their remarkable photostability.[49,50] Chemically, the community considered that the precursor of this red pigment is naphthazarin (5,8-dihydroxy-1,4-naphthoquinone), a naturally occurring 1,4-naphthoquinone derivative.[51,52] Most natural naphthoquinones are plant products, while a few can be found in sea urchins or elaborated by microorganisms (commonly isolated from fungi).[53] The chemical structure of Draconin Red is characterized by its high degree of symmetry as well as one conjugated system across two aromatic rings (see Section 3.1).[50] The properties of Draconin Red have thus far been rarely studied, but the dye is known to share several promising properties with the more fully investigated xylindein, similarly secreted by a spalting wood fungus.[35,37,50,54,55] Both pigments display high thermo- and photostability, a broad absorption profile spanning the visible spectral range, and a largely symmetric structure comprised of conjugated rings with polar carbonyl and hydroxyl group substituents, which may preserve the chromophore's ability to participate in intermolecular hydrogen (H)-bonding in solution aggregates or thin films.[37,56] Draconin Red exhibits a large Stokes shift and a low fluorescence quantum yield (e.g., FQY≈1.41% in ethanol, see Section 2.3), both of which are characteristic of a proton transfer relaxation pathway in ESIPT dyes.[38,57]

In this work, we implemented a suite of steady-state and time-resolved spectroscopic techniques from electronic absorption and fluorescence, femtosecond transient absorption (fs-TA), femtosecond stimulated Raman spectroscopy (FSRS), aided by quantum calculations, to elucidate the reversible ultrafast ESIPT reaction between two tautomers of Draconin Red in two different solvents (dichloromethane and dimethyl sulfoxide) under two strategically chosen excitation wavelengths of 510 and 537 nm. A characteristic sub-picosecond time constant was identified as the rate-limiting step for photoinduced interconversion between two tautomers, accompanied by other longer excited-state processes including solvation, rotational motions, and nonradiative relaxation. With deep structural dynamics insights of Draconin Red in solution on ultrafast timescales, we proposed rational design and molecular engineering principles to improve Draconin Red as a sustainable functional material with potential photonics and optoelectronic applications.

2. EXPERIMENTAL AND COMPUTATIONAL METHODS

2.1. Preparation of Draconin Red. The red pigment was produced, extracted, and purified based on the methods given in previous reports.[50,58,59] In brief, *Scytalidium cuboideum* (Sacc. & Ellis) Sigler & Kang (UAMH 11517) cultures were grown on 2% malt agar (VWR) plates amended with white-rotted maple wood chips following established methods.[60] The cultures were grown for six weeks until media was fully pigmented, then allowed to air dry and ground with an Oster blender (Model 6811). Pigment was extracted from the resulting powder by addition of 99.9% HPLC-grade acetone (VWR), then stirred at room temperature (20 °C), and filtrated with 415 filter paper (VWR). Pigment solution was then concentrated using Büchi Rotavapor (Model 461) in a 40 °C deionized water bath. Crystals were precipitated using liquid nitrogen as outlined in our previous report[50] and collected by filtration (415 filter paper, VWR). The crystals isolated using this method, which have been known to be of very high purity (99.9%),[58] were subsequently redissolved in acetone and could be isolated by extracting suspended crystal clumps with tweezers. To our best knowledge, Draconin Red has not been made via organic synthesis, thus lending significance to the extraction and characterization of this naturally occurring dye molecule.[52,53]

2.2. Steady-State Electronic Spectroscopy. For steady-state and time-resolved spectroscopic measurements (see below), Draconin Red was used as is following the extraction and purification of the pigment from the fungus *Scytalidium cuboideum* (Section 2.1). To dilute the sample to achieve suitable concentrations for various spectroscopic measurements, the lab-grade solvents dichloromethane (99% purity, TCI), dimethyl sulfoxide (EMD), and ethanol (Koptec) were used when necessary without future filtration. A Thermo Scientific Evolution 201 UV/Visible (UV/Vis) spectrophotometer and a Shimadzu RF-6000 Spectrofluorophotometer were used to measure the steady-state absorption and emission spectra of sample solution, respectively. For these electronic absorption and emission measurements, a 1 mm pathlength quartz cuvette (Spectrosil 1-Q-1, Starna Cells) and a four-sided rectangular quartz cuvette with a 5 mm pathlength were used, respectively, the latter setup also being used for the FQY measurement (Section 2.3).

2.3. Fluorescence Quantum Yield Determination. A dry sample of Draconin Red was dissolved in 99% pure ethanol (Koptec), and further diluted with ethanol until the measured sample absorbance was below 0.1 OD (optical density) per 5 mm to avoid any aggregation or inner filter effects.[61] Once sample absorbance was acceptable, a Shimadzu RF-6000 Spectrofluorophotometer was used to measure fluorescence intensity with 500 nm excitation, and the integrate peak area for emission intensity was obtained in the 600–700 nm range (or 560–650 nm for other solvents). The peak areas were plotted against the values of $(1 - 10^{-OD})$ from absorbance measurements for the percentage of absorbed photons by the sample solution.[62] This process was then repeated using the 4-(Dicyanomethylene)-2-methyl-6-(4-dimethylaminostyryl)-4*H*-pyran (DCM) reference dye in ethanol, which has a usable excitation range of 400–530 nm and emission range of 560–700 nm.[63] Both datasets were fit with a linear trendline with an intercept of zero (representative spectral data shown in the SI). The resulting slope of each dataset (S_{DR} and S_{DCM}), along with the known standard FQY of the DCM dye ($\Phi_{DCM} = 0.435$) and solvent refractive index (n_{DR} for Draconin Red and n_{DCM} for DCM dye), were used in the following equation to determine the FQY of

Draconin Red (Φ_{DR}) in various solvents (ethanol, dimethyl sulfoxide, and dichloromethane) investigated in this work,

$$\Phi_{DR} = \frac{S_{DR}}{S_{DCM}} * \Phi_{DCM} * \frac{{n_{DR}}^2}{{n_{DCM}}^2} \tag{1}$$

2.4. Femtosecond Transient Absorption (fs-TA) and Femtosecond Stimulated Raman Spectroscopy (FSRS). A detailed description of the wavelength-tunable fs-TA and FSRS setups can be found in our prior reports.[28-30,64,65] Briefly, the fs-TA setup was based on the fundamental laser output pulse train (~800 nm center wavelength, 35 fs pulse duration, 1 kHz repetition rate, ~3.6 W average power) from a regenerative amplifier (Legend Elite-USP-1K-HE, Coherent, Inc.) seeded by a mode-locked Ti:Sapphire oscillator (Mantis-5, Coherent, Inc.). The fs probe was generated by passing a small portion of the laser output through a 2-mm-pathlength quartz cuvette filled with deionized water. The supercontinuum white light was then reflected 11 times in a chirped-mirror pair (dispersion compensating mirror: DCM-9, 450–950 nm, Laser Quantum, Inc.) for optimal compression to <100 fs full-width-at-half-maximum (FWHM) of pulse duration.[65]

For photoexcitation, the fs actinic pump was produced from a two-stage noncollinear optical parametric amplifier (NOPA) system with the first NOPA generating the desired wavelength and the second one amplifying the power. Subsequently, the laser beam went through a chirped-mirror pair (DCM-12, 400–700 nm, Laser Quantum, Inc.) and reflected 9 times to achieve the shortest pulse duration. Fs-TA measurements were performed with both the parallel and magic-angle (54.7°) polarizations between the actinic pump and probe beams. In practice, the polarization of the probe was first determined by placing a polarizer and a white paper afterwards in its beampath. The polarizer was rotated until the transmitted probe became the weakest. The same polarizer was then placed in the pump beampath between a half-waveplate (zero-order, WPH10M-514, Thorlabs, Inc.) and a power meter (PM100D meter with S302C thermal power sensor head, Thorlabs Inc.), and the power of transmitted pump was monitored by rotating the waveplate until the lowest power was observed. Under this condition, the polarizations of the pump and probe were parallel. The half waveplate could then be rotated by ~27.4° (while the polarizer was removed) to achieve the magic-angle condition in order to minimize the molecular rotational contributions to the observed TA dynamics and photoselection effects.[11]

The pump and probe beams were focused by a parabolic mirror onto 1-mm-pathlength quartz cell filled with the sample solution. For red pigment dissolved in dichloromethane (DCM solvent), the sample was stirred by a magnetic stir bar (homemade using a miniature staple fragment) to avoid sample degradation at the same laser spot and ensure fresh sample was irradiated during the entire data collection. For red pigment in dimethyl sulfoxide (DMSO solvent), the cuvette position was slightly changed by the experimenter throughout the data collection because interactions between DMSO and a zinc-plated steel piece (likely as a reducing agent) could deprotonate the chromophore sample. Past the sample cell, the probe was then collimated, focused into a spectrograph (IsoPlane SCT-320, Princeton Instruments, Inc.), dispersed inside by a reflective grating (300 groves/mm, 300 nm blaze wavelength), and imaged onto a CCD array camera (PIXIS:100F, Princeton Instruments, Inc.). The fs-TA spectra of red pigment were taken with both 510 and 537 nm photoexcitation in DCM and DMSO solvents from –2 ps to 900 ps with uneven time steps. The pump power was set at ~0.3 mW, measured before the chopper that was synchronized with the main laser clock but at half of the laser repetition rate (i.e., 500 Hz).

For ground-state (GS) and excited-state (ES)-FSRS experiments, the tunable actinic pump and white light probe were generated and compressed similarly to the aforementioned description of fs-TA measurements. A tunable picosecond (ps) Raman pump was implemented in conjunction with the actinic pump and Raman probe, making ES-FSRS a pump-pump-probe technique in the mixed time-frequency domain.[18,30] A home-built NOPA system was implemented to generate the narrowband Raman pump in three stages. First, we used an fs-NOPA to provide the seed pulse by focusing supercontinuum white light and fs 400 nm pulses on a beta-barium-borate (BBO) crystal. At the suitable phase-matching condition, the output seed of the desired wavelength was dispersed using a grating and directed into a slit-based spectral filter to become a narrowband (ps) seed. For the ensuing two-stage NOPAs, the fs 800 nm pulses were first converted to ps 400 nm pulses using a home-built second harmonic bandwidth compressor (SHBC).[64] The ps 400 nm pulses were used as optical pumps in two ps-NOPAs to amplify the aforementioned seed at the desired wavelength. For GS-FSRS measurements, only the ps Raman pump and fs Raman probe were directed onto the sample to collect the Raman spectrum at thermal equilibrium. Several Raman pump wavelengths were used to resonantly stimulate[30,66] the Stokes (redder Raman probe than Raman pump) FSRS spectra of both tautomers of Draconin Red, which included 530, 550, and 600 nm Raman pumps with average powers of ~4.4, 4.0, and 3.0 mW, respectively. For the anti-Stokes (bluer Raman probe than Raman pump) ES-FSRS measurement, a 537 nm actinic pump and 645 nm Raman pump were employed at powers of ~0.25 and 2.2 mW, respectively. The spectrograph grating used for FSRS was 1200 groves/mm (much higher spectral resolution than fs-TA) and 300 nm blaze wavelength to disperse and direct the transmitted probe pulse onto the CCD camera. FSRS measurements were all taken in 1-mm-pathlength quartz cuvette with a magnetic stir bar. To directly contrast with FSRS spectrum on the Stokes side, the FSRS spectrum collected on the anti-Stokes side needs to be multiplied by –1 in both the intensity and Raman shift axes.[29,30]

For fs-TA measurements on Draconin Red in both solvents (DCM and DMSO), the sample concentrations were adjusted to set the absorbance (OD) as ~1.0/mm at 510 nm for both 510 and 537 nm excitations. For GS and ES-FSRS in DCM, the same sample concentration was used with

530, 550, and 600 nm Raman pumps. The UV/Vis spectra were collected before and after each ultrafast measurement to confirm the sample photostability over the course of experiments.[16,28]

2.5. Quantum Calculations. The ground state (S_0), unrelaxed excited state (S_1), and relaxed excited state (S_1') quantum calculations on the two tautomers of Draconin Red were performed using Gaussian 09 software.[67] The energies for the respective states depicted in the potential energy surfaces (PESs, see Section 3.6) were retrieved using the density functional theory (DFT) and time-dependent (TD)-DFT methods for S_0 and S_1 calculations, respectively. In particular, the S_0 energy was taken directly from the DFT optimization of both tautomers (atomic coordinates listed in the SI Appendix). The unrelaxed S_1 energy was determined by performing TD-DFT energy calculation on the ground state optimized tautomers. The relaxed S_1 energy was taken from the TD-DFT geometric optimization of both tautomers. For all calculations, the B3LYP functional and 6-311+G(d,p) basis set were used with default solvent parameters of the integral equation formalism variant within the polarizable continuum model (IEFPCM) to represent the DCM solvent.

To determine the transition barrier height for ESIPT within the relaxed excited state and model the tautomerization of Draconin Red, a 2D scan of pertinent –OH bond distances was performed. TD-DFT optimizations were performed with the aforementioned functional/basis set in DCM (implicit solvation using IEFPCM) to reduce computational costs. The starting conformation was the PA tautomer (see Section 3.1), both the –OH coordinates were scanned with 0.1 Å steps from 1 to 2 Å (Section 3.4). A relaxed scan was performed with 121 TD-DFT geometrical optimizations in total. For the contour plot of 2D scan, the minimum energy states representing PS tautomer were set to zero. The corresponding higher-energy states were subtracted by the energy of the lowest-energy state to plot on a representable scale. A similar scan beginning with the PS tautomer was performed, producing a mirror-like contour plot due to the symmetry of Draconin Red structure.

2.6. Franck-Condon/Herzberg-Teller Calculations. The structures for each tautomer were recreated in GaussView 6 and optimized using DFT-B3LYP/6-311+G(3df,2p) and the IEFPCM solvation model for Draconin Red in DCM; the theory level, basis set, and solvation parameters were specified in all calculations prerequisite to the Franck-Condon/Herzberg-Teller (FCHT) calculations using Gaussian 16 software.[68] The resulting geometry checkpoint files were then referenced (using the "OldChk" keyword to preserve contents) in two more calculations. First, the optimized geometry was read to calculate vibrational normal modes of the ground state of each tautomer (see the associated Raman results in Section 3.5). The normal mode information was kept in the checkpoint file using the "SaveNM" keyword. Second, the S_1 state geometry was calculated using TD-DFT with the optimized S_0 geometry as a starting point. The resulting geometry was then used in a frequency calculation in the same fashion as the ground state.

The checkpoint files resulting from the ground and excited state frequency calculations were used in FCHT calculations, with instructions to print spectra with a grain of 5 cm^{-1} and use absolute wavenumber bounds, yielding spectra with identical wavenumber axes. This step was required by the summation step in the one-photon absorption (OPA)/one-photon emission (OPE) analysis, so the scaling used for each tautomer could be identical. Two FCHT calculations were performed for each tautomer: one for excitation to the S_1 state, and one for relaxation to the ground state (S_0).

3. RESULTS AND DISCUSSION

Similar to another naturally occurring organic dye Alkannin (from the borage family *Alkanna tinctoria*), Draconin Red possesses two sites wherein ESIPT can occur: keto-enol tautomerization is possible between the functional groups at positions 4 and 5 and/or 1 and 8 on the naphthazarin ring system (Figure 1a), also providing a pathway for excited-state intramolecular double proton transfer (ESIDPT, see below).[69] Most interestingly, a particularity of Draconin Red arises from its highly symmetric structure: keto-enol tautomerization at C4 and C5 positions results in the identical structure as tautomerization at C1 and C8 positions, while ESIDPT would result in a return to the original structure irrespective of the sequence of site tautomerization. The detailed investigation of an intrinsically coherent and ultrafast ESIPT reaction process and the participation of ESIDPT thus became a focus of this work. Previous work also reported two distinct (red and orange) needle-like crystals that can be readily produced by the *Scytalidium cuboideum* fungus with a simple cold acetone extraction,[50] contrasting the *Chlorociboria* fungus-secreted xylindein that makes amorphous thin films but not crystals.[35,55] Relevant discussions on more practical applications (Section 3.7) will follow the comprehensive ultrafast spectral analysis from steady-state electronic (Section 3.1) as well as time-resolved electronic (Section 3.2–3.3) and vibrational (Section 3.5) spectroscopy, quantum calculations (Section 3.4), and PES discussions (Section 3.6).

3.1. Steady-State Electronic Spectroscopy and Elucidation of Two Conformers. Using an integral characterization platform from experiments to computations, we aim to reveal the primary events that power the photochemistry of this underexplored red pigment. To delineate the ultrafast photoresponse of Draconin Red on its intrinsic molecular timescales,[18] the broad and convoluted steady-state electronic spectra (Figure 1b,c) must be first disentangled to resolve the chemical/molecular species present in solution. The absorption spectrum of Draconin Red in DCM spans the visible spectrum from ca. 400–600 nm and extends into the ultraviolet region, with three prominent peaks at ~550, 510, and 480 nm. In ethanol and DMSO, solvatochromism slightly blue-shifts (by ~2 nm) these peaks, while red-shifting the emission peaks by ~10 nm (Figure S1), indicating the possibility of a CT state that becomes stabilized in more polar solvents, particularly with the enhanced H-bonding interactions in DMSO.[70-74] For corroboration, the inhomogeneous broadening of the steady-state spectral profiles is apparent when Draconin Red is dissolved in

DMSO (Figure S1) that is more polar than DCM,[71,75] showing an increased ~576 nm emission relative to the main ~618 nm emission peak in DMSO versus that in DCM (Figure 1c). Notably, the solubility of the red pigment is reduced in more polar solvents, especially ethanol and water, implying that the interplay between (nonspecific) polarity and (specific) H-bonding interactions exerts a complex effect on equilibrium and non-equilibrium properties of Draconin Red.

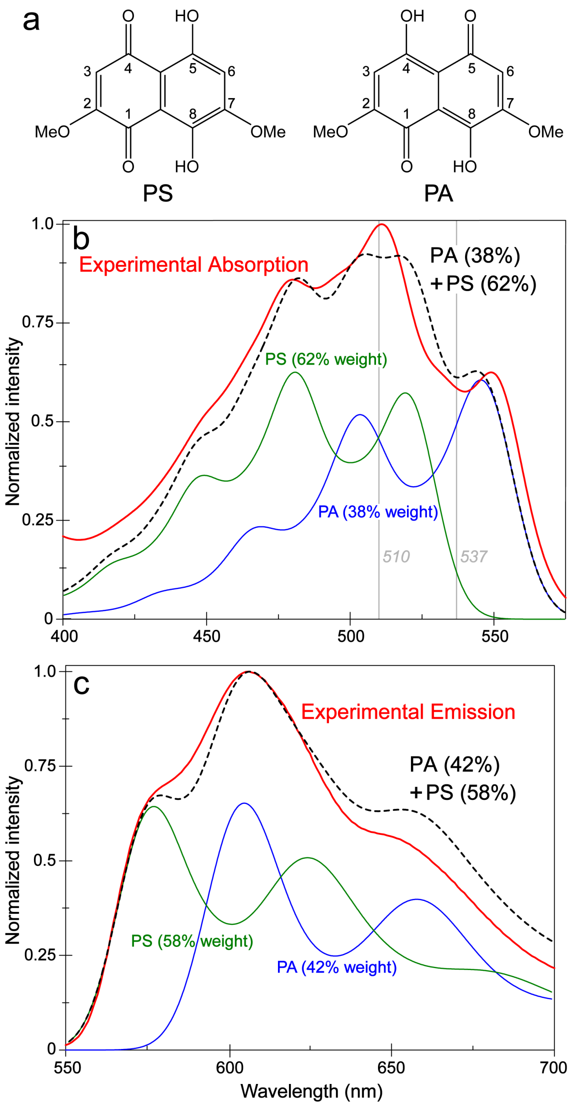

Figure 1. Chemical structure and steady-state electronic spectra of Draconin Red in DCM. (a) The para-symmetric (PS) and para-antisymmetric (PA) chromophores with key functional group atomic sites numbered. The electronic (b) absorption and (c) emission spectrum (red) can be fit to

two conformers, PA (blue) and PS (green) with the associated amplitude weights listed in parentheses, with spectral summation depicted in black dashed lines. Two excitation wavelengths at 510 and 537 nm for transient absorption measurements are denoted by vertical lines in panel b.

Previous experimental and theoretical studies found that many tautomers involving various orientations of hydroxy groups may exist in solution, similar to other naturally derived molecules like xylindein and hypericin.[50,55,76] Quantum mechanical modeling deduced that two tautomers constitute a majority of the species, referred to as the para-antisymmetric (PA) and para-symmetric (PS) tautomers with two hydroxy groups located on the opposite and same sides of the center bond, respectively (Figure 1a), while both –OH groups point toward the adjacent C=O groups for energy stabilization. Regardless of the level of theory or basis sets, PA with a centrosymmetric core consistently absorbs redder than PS (Figure 1b). Although PS absorbs in the bluer region, its calculated ground state (S_0) energy is lower than PA by 0.162 eV while the calculated absorption transition oscillator strength of PA (0.2145) is higher than PS (0.1772). Using Gibbs free energy equation for a system undergoing tautomerization at chemical equilibrium, $\Delta G^\circ = -RT \ln K_{eq}$, we estimated that PS energy is lower than PA by ~0.025 eV at room temperature (22 °C) from the OPA spectral fits, which is within a factor of 2 compared to the previously reported free enthalpy of the tautomerization reaction between two conformers of alizarin (similar-sized organic chromophore) in the ground state.[77] Therefore, the bluer absorption peak at ~510 nm attributed to PS is significantly more intense than the red-shifted peak at ~550 nm because PS is the more stable species at equilibrium, even while considering the difference in oscillator strength. Possible resonance structures (Figure S2) indicate that the PS tautomer is better able to access the stabilizing effects of electronic conjugation with two structures in which no atom takes on a formal charge.

Vibronic coupling is ubiquitous for many π-conjugated organic molecules, commonly arising from skeletal C=C stretching and ring-breathing motions that lead to shoulder peaks and a broadened absorption profile.[17,78,79] To dissect the steady-state spectra and aid the interpretation of excitation-dependent ultrafast spectroscopic measurements (see below), a rigorous analysis of vibronic progression is warranted with a quantum mechanical foundation.[80-83] We performed an FCHT calculation representing excitation to the first singlet excited state (S_1) for each tautomer (see Section 2.6), and predicted the one-photon absorption and emission spectra (Figure 1b,c).[84,85] The wavenumber axis of each spectrum was multiplied by a scaling constant of 1.12 and 1.02 for absorption and emission, respectively, thus representing a blueshift to match experimental values and then converted to the wavelength unit. The pertinent blueshift magnitude of ~0.25 and 0.05 eV to match the calculated absorption and emission spectra with experimental spectra of Draconin Red is well within the commonly used blueshift of ~0.2–0.5 eV for organic molecules[80] and similar chromophores like naphthalene.[86] The intensities of the calculated tautomer spectra were scaled by the empirically determined weighting constants ($C_{\mathrm{Abs,PA}} = 0.62$, $C_{\mathrm{Abs,PS}} = 1$; $C_{\mathrm{Em,PA}} = 0.73$, $C_{\mathrm{Em,PS}} = 1$), which produced the best agreement with the intensities of three peak maxima in the experimental absorption and emission spectra (separately). The scaled tautomer spectra were summed to produce a weighted spectrum, which could be directly compared to the measured spectrum when normalized. Notably, the relative weights of PA (38%) and PS (62%) that produced the best agreement with measured peak intensities (Figure 1b) qualitatively match the predicted S_0 population preference of PS over PA. The blue shoulder peak at ~480 nm (near the primary peak at ~510 nm) is due to vibronic coupling with contributions from both tautomers, primarily PS according to the OPA analysis. The red shoulder peak at ~550 nm appears to be primarily associated with PA with minimal contribution from PS (Figure 1b).

Though a broader peak width (700 cm^{-1} FWHM) appeared to produce a more visual agreement with the experimental electronic spectra (Figure 1b,c), calculations performed with default broadening parameters (FWHM=270 cm^{-1}, see Figure S3) correlate to relative weights of PA=30% and PS=70% that further supports the PS population dominance in S_0 (Figure S3a). This disparity of retrieved population ratios implies that any further broadening of the spectral components is due to coupling effects between the two tautomers, either equilibrated or dynamically interchanging, possibly aided by π-π stacking interactions between conjugated rings of adjacent molecules, which could cause them to act more like a single absorbing system and manifest one broad absorption profile with multiple shoulder peaks.

A mirror-like symmetry is also apparent upon comparing the absorption and emission spectra, which implies a rigid molecular structure. For Draconin Red in DCM, three emission peaks are located at ~575, 600, and 650 nm with the middle peak being the most intense (Figure 1c). Reminiscent of the absorption spectrum, PS is calculated to emit in the bluer region with a Stokes shift of ~1910 cm^{-1} while PA emits redder with a reduced Stokes shift of 1760 cm^{-1}, aided by the OPE calculations that represent the radiative transition from S_1 state. The individual and cumulative OPE spectra reveal that the pronounced shoulder band observed above 650 nm is primarily due to PA species, in contrast to the absorption shoulder peak at ~480 nm.

A rather interesting trend was obtained by comparing relative percent weights of the absorption and emission spectra. The cumulative OPE fit shows a shift toward an even distribution of tautomer populations, PA (42%) and PS (58%), contrasting the larger (62%) contribution from PS in the OPA fit. This trend remains after considering the downward transition oscillator strength of PA* (0.2353) and PS* (0.1966). The changed ratio could be owing to ESIPT, which both tautomers undergo to effectively dissipate the photoexcitation energy. Ultrafast measurements and more in-depth quantum calculations are required to examine ESIPT reactions, wherein photoexcitation of PS results in transient formation of PA and vice versa. Since PS is energetically favored and represents majority of the equilibrium population, excitation of this form results in a relatively larger PA excited-state population (via ESIPT), hence the aforementioned PA/PS population ratio change. The FQY was measured to be 1.41% upon 500 nm excitation of Draconin Red in ethanol (Figure S4), suggesting that effective nonradiative pathways may be opened by shifting the proton between the adjacent carbonyl and hydroxy groups.[39]

Interestingly, for Draconin Red in the other two solvents, a bluer integration region of fluorescence band (e.g., 560–590 nm in DCM and 560–600 nm in DMSO) consistently shows a higher FQY than a redder integration region (e.g., 590–650 nm in DCM and 600–650 nm in DMSO). Besides being consistent with a bluer excitation at 500 nm that mainly pumps PS, this result also suggests that PS* is more fluorescent than PA*. With a reduced downward transition oscillator strength of PS* compared to PA*, our finding affirms that PS is the dominant species at thermal equilibrium, and the PS*→PA* conversion is likely a less favorable ESIPT pathway compared to PA*→PS*. We then repeated the steady-state emission measurements using 530 nm excitation for Draconin Red in DCM, and observed a slight increase/decrease of the fluorescence intensity within 560–590 nm/590–650 nm compared to the 500 nm excitation case. This result is rather unexpected because a redder excitation light can pump more PA (Figure 1b) and should lead to less PS*/more PA* emission in bluer/redder regions. Taken together, these fine steady-state emission data analysis supports that PA*→PS* is the more favored pathway in the excited state (see below for more spectral support). Notably, this efficient energy dissipation pathway via ESIPT reaction was observed for a related fungal pigment, xylindein;[35] however, the FQY of xylindein (<0.1% in DCM after 532 nm excitation) was observed to be lower than Draconin Red (3.66% and

3.37% in DCM after 500 nm and 530 nm excitation, respectively) by more than an order of magnitude.[37,56]

3.2. Fs-TA Spectroscopy Tracks Ultrafast ESIPT Reaction. While the insights gained from steady-state measurements and quantum calculations serve as a solid foundation, a burning question remains unanswered: do both tautomers undergo ESIPT and what is the timescale for this process? To help delineate this unexpectedly complex problem due to the spectrally overlapping and structurally similar tautomers (Figure 1a), ultrafast coherent electronic measurements in the form of femtosecond transient absorption (fs-TA) were performed in two representative solvents, DCM and DMSO, with two strategically selected excitation wavelengths of 510 and 537 nm (Figure 2).

Aided by the aforementioned OPA calculations (Section 3.1), 510 nm excitation primarily pumps PS whereas the redder excitation (537 nm) is more resonant with PA (see Figure 1b). However, both actinic pump wavelengths can excite each tautomer to varying degrees due to their similar $S_0 \rightarrow S_1$ transition energies, the broadness of absorption spectra in solution, and the bandwidth of the fs pump pulse used in fs-TA. In all four 2D-contour plots of the fs-TA spectra (Figure 2a,b,e,f), transient electronic spectral features consist of a broad stimulated emission (SE) band from ~550–700 nm with multiple discernible peaks. Similar to steady-state fluorescence emission profile of Draconin Red (see Figure 2c in DCM and Figure 2d in DMSO), the SE band manifests three peaks around 555, 615, and 650 nm that can be attributed to the downward $S_1 \rightarrow S_0$ transition originating from PS, PA, and a vibronic coupling band of PA, respectively. Note that the 555 nm SE band could have ground-state bleaching contributions from PA (Figure 1b), while the 650 nm vibronic band displays similar dynamics as the main fluorescent peak of PA* (see blue trace in Figure 1c).[18,87] All the observed SE peaks display a redshift on the ps timescale, which is more prominent in DMSO (Figure 2b,f) than that in DCM (Figure 2a,e). An excited-state absorption (ESA) feature was observed below 500 nm using a bluer probe window, likely with contributions from both tautomers of Draconin Red.[18]

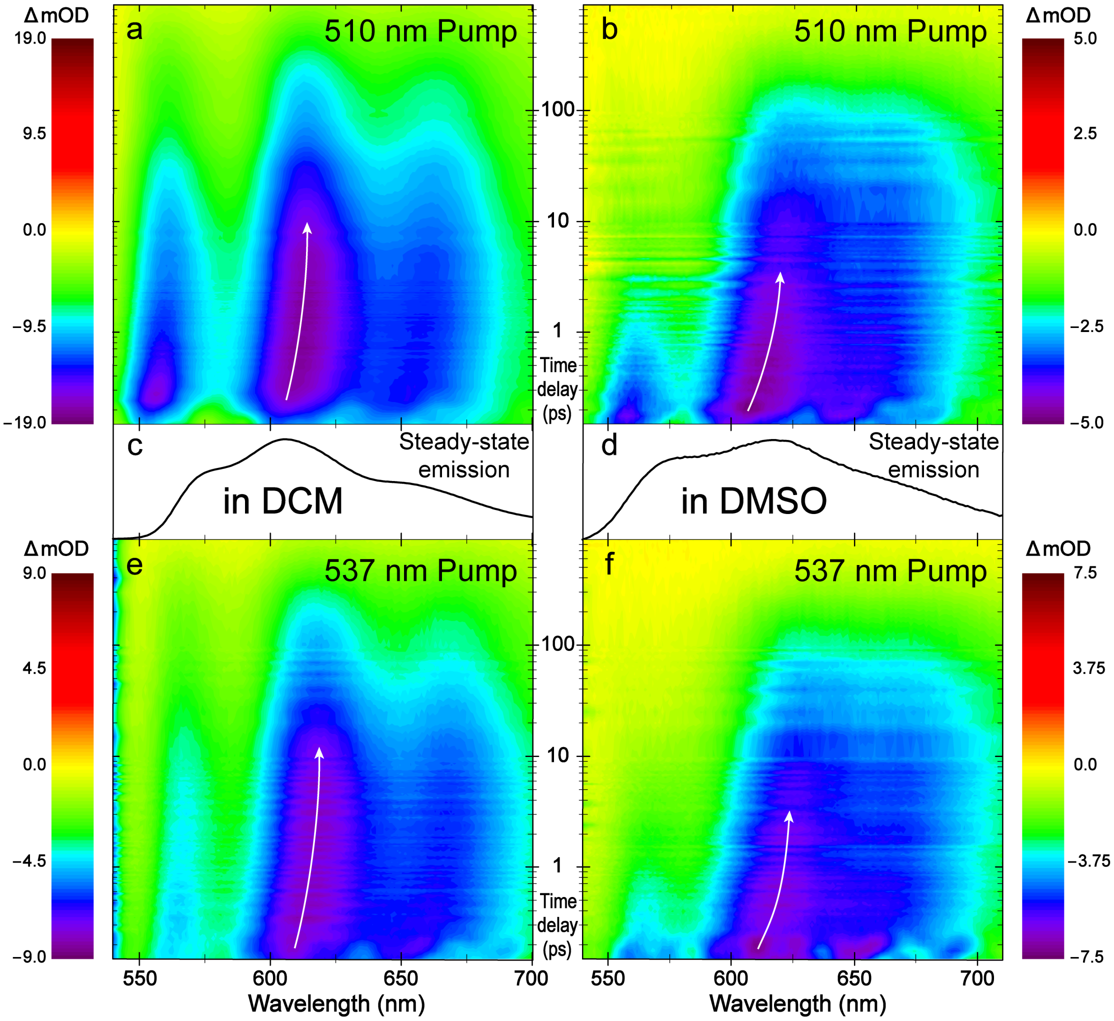

Figure 2. Contour plots for the excitation-dependent fs-TA spectra of Draconin Red in various solvents. With (a)/(b) 510 nm and (e)/(f) 537 nm actinic pump, Draconin Red in DCM/DMSO shows prominent TA bands that correlate with (c)/(d) steady-state emission spectrum, respectively. The ultrafast stimulated emission peak redshift is highlighted by the white curved arrow.

To provide more in-depth information about the contributing tautomers, we focused on the intensity dynamics of two peaks at ~555 nm (mainly PS) and 610 nm (mainly PA) and found that the two tautomers undergo notably different energy dissipation pathways as shown in Figure 3. A suitable integral wavelength range was selected to cover the bluest SE peak at early times and reddest SE peak at later times to minimize effects of peak wavelength shift on intensity dynamics, which remain as the focus here for the visually separated PS* and PA* emissive species (see Figure 2). Regardless of the solvent or excitation wavelength, the bluer SE feature of Draconin Red decays with a sub-ps time constant of ~640–750 fs while this decay only occurs for the redder SE feature during one experimental condition (510 nm excitation in DMSO, Figure 3b). According to the assignment of these features, the dynamics suggest that PS (blue traces in Figure 3) may undergo an efficient energy dissipation pathway not readily observed for PA (red traces in Figure 3) following actinic photoexcitation.

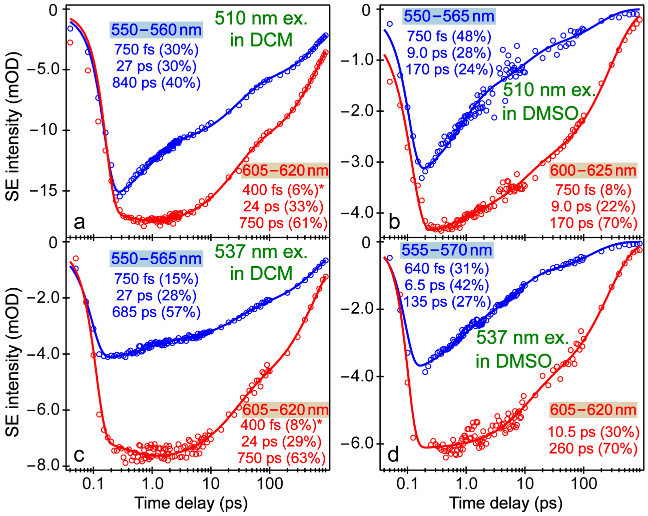

Figure 3. Transient electronic dynamics of Draconin Red under various conditions. The probe-dependent intensity dynamics in DCM using (a) 510 nm and (c) 537 nm actinic pump and in DMSO using (b) 510 nm and (d) 537 nm actinic pump show interesting comparative patterns. The initial rise component with ~400 fs time constant for the redder stimulated emission features in panels a and c (red curves) is denoted by an asterisk. The best fits are shown as solid curves.

There are a few key observables from the probe-dependent intensity dynamics that help unlock the PESs of both tautomers. For both excitations in DCM (Figure 3a,c), a conserved "intermediate" 24–27 ps time constant carries an amplitude weight of ~30%. Based on similar dynamics for many rigid photosensitive molecules, it was surmised that this decay stems from molecular rotational motion in solution.[88,89] The time constant for such processes can be estimated using Debye Theory according to the following equation:[62]

$$\tau_{rot} = \frac{1}{6D_{rot}} = \frac{\eta V}{k_B T} \tag{2}$$

Several variables play a role in calculating the rotational motion timescale, most important in the current investigation are the solvent viscosity and solute volume. To calculate the latter, a spherical molecule is considered insufficient as an accurate representation because Draconin Red has two methoxy groups protruding on both sides of the structure. Therefore, the long and short axial diameters of 11.16 and 6.12 Å were taken from the optimized DFT-B3LYP calculations on Draconin Red to determine the molecular volume. Using the solvent viscosity of DCM (0.413 centipoise or cP, 1 cP = 1 mPa·s) at 20 °C, the estimated rotational time constants are 74 and 12 ps about the two axes, respectively. Notably, the average of these time constants (43 ps) largely matches the intermediate decay observed during fs-TA experiments. Alternatively, if we consider an oblate spheroid with a horizontal semi-axis of 5.58 Å and vertical semi-axis of 3.06 Å, the volume can be obtained as ~399 Å^3, leading to a rotational time constant of ~41 ps.

To provide further evidence for the assignment of rotational motion, magic-angle experiments were performed on the red pigment by placing a waveplate in the actinic pump beampath to set its polarization to ~54.7 degrees with respect to the *p*-polarized probe (from supercontinuum white light), which removes the contribution of solute rotational motion from the TA signal intensity dynamics (Section 2.4).[90,91] For both excitation wavelengths in the magic-angle TA spectra, the intermediate decay component (~25 ps) is noticeably absent, corroborating its assignment to the solute rotational motion (see Figure S5 for the representative 510 nm excitation case). Interestingly, a delayed rise of the SE band was observed from ~10–100 ps under the magic-angle polarization conditions, which can be further investigated by performing additional parallel/perpendicular polarization-dependent experiments to plot the anisotropy dynamics.[92] The remaining intensity decay/rise components are similar to the aforementioned dynamics (Figure 3), confirming that they are not directly affected by rotational contributions.

In DMSO, rather different dynamics were observed with a 6.5–10.5 ps intermediate decay time constant on a shorter timescale than the Draconin Red rotational motion in DCM. The viscosity of DMSO (2.0 cP) is significantly larger than DCM, leading to a larger rotational time constant using Equation (2), hence it is unlikely that this particular time constant represents the rotational motion. The intermediate decay dynamics are reminiscent of the fs-TA dynamics observed for a similar-sized organic molecule, 8-methoxypyrene-1,3,6-trisulfonate (MPTS).[28,62,93] In DMSO, the ESA peak of MPTS blue-shifts on the ~5 ps timescale assigned to solvation of the hot photoexcited molecule. Therefore, the intermediate decay component observed for Draconin Red in DMSO likely involves vibrational cooling aided by solvation.[28,29,94] Such a solvation component may not be present in DCM (CH_2Cl_2), since this solvent can only form weak bonds to the carbonyl groups of Draconin Red given the H-bond donating/accepting strength of DCM (0.30/0.0).[70] Conversely, the sulfoxide group of DMSO could form stronger H-bonds to the hydroxy groups of Draconin Red according to the DMSO H-bond donating/accepting strength (0.0/0.76). The increased solute-solvent H-bonding is reflected by the red-shifted steady-state emission profile of Draconin Red in DMSO (Figure S1) compared to DCM. This difference in H-bonding properties of the respective solvents has interesting impacts on the ESIPT pathway as will be discussed in later sections.

A comparison of the TA intensity dynamics on the hundreds-of-ps timescale in both solvents informs two different stories. In DCM, the red pigment decays on the relatively long timescale of 685–840 ps, likely representing an apparent fluorescence lifetime (see Section 3.7 for related data in crystals).[62,74] An average of nonradiative and radiative transitions, this time constant provides a reliable marker that can be connected to the solute chromophore FQY. Typically, molecules with a large FQY display a relatively longer apparent fluorescence lifetime approaching true lifetime of the fluorescent state in comparison to molecules with a small FQY.[95] For reference, xylindein has an order of magnitude lower FQY (<0.1%) than the red pigment and hence has a reduced excited-state lifetime of ~30 ps due to the flexible scaffold of the larger xylindein molecule acquiring a butterfly-like shape, potentially leading to an S_1/S_0 conical intersection that rationalizes the low FQY.[35] The more rigid structure of red pigment (Figure 1a) restricts such large-scale out-of-plane motions and thus leads to MPTS-like dynamics.[62] In DMSO, a much-reduced time constant ranging from 135–260 ps likely represents the lengthened rotational motion in the more viscous solvent (2.0 cP of DMSO) supported by the calculated Debye relaxation time constant of 197 ps using Equation (2) for an oblate spheroid. The absence of a longer time constant approaching the typical nanosecond (ns) fluorescence lifetime in DMSO supports several reports showing that solute-solvent H-bonding may quench radiative processes (also see Figure S4 and related discussions).[96-98] Additional magic-angle measurements yielded a longer time constant of ~400 ps which suggests that the apparent hundreds-of-ps time constant in DMSO (Figure 3b,d) may well contain some contributions from other nonradiative relaxation pathways back to S_0.

3.3. Global Analysis of Fs-TA Spectra Highlights Inhomogeneous Populations. Overall, the probe-dependent intensity dynamics (Figure 3) on the basis of deconvoluted tautomers from steady-state electronic spectra (Figure 1b,c) are reflected in the evolution-associated spectra (EAS) retrieved from global analysis[11] of the respective fs-TA spectra (Figure 4) using the open-source Glotaran software.[99] The clear redshift of SE feature in DMSO on the intermediate timescale (7–12 ps, red→blue in Figure 4b,d) supports the vibrational cooling assignment aided by solvation, which leads to a relaxed excited state.[18] In contrast, the lack of a redshift during the intermediate stage (21–27 ps, red→blue) in DCM (Figure 4a,c) shows that solvation does not significantly impact the rotational motion of Draconin Red in this solvent.

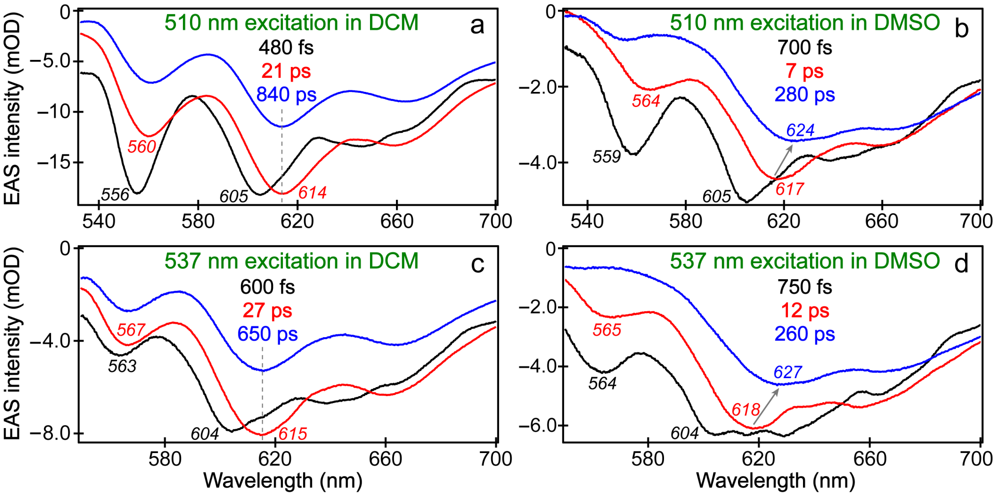

Figure 4. Evolution-associated spectra (EAS) from global analysis of fs-TA spectra of Draconin Red using (a)/(b) 510 nm and (c)/(d) 537 nm actinic pump in DCM/DMSO, respectively. The temporal components evolve from black→red→blue with associated time constants listed in the inset. Key stimulated emission (SE) peak shifts are indicated by gray arrows in panels b and d, while the unchanged peak position at ~615 nm is denoted by vertical dashed lines in panels a and c. The multiple SE peak positions in nm units are labeled by their respective locations.

Moreover, relative intensities of the ~555 and 610 nm SE peaks are altered with the excitation wavelength. By calculating the intensity ratios using initial SE magnitudes from Figure 2, the following values were determined: 510 nm excitation in DCM (93%) and DMSO (77%), 537 nm excitation in DCM (52%) and DMSO (58%). For example, around time zero for Draconin Red in DCM with 510 nm excitation (Figure 2a), the 555 nm peak intensity is –15.5 mOD while the 610 nm peak intensity is –16.6 mOD (i.e., 15.5/16.6 ≈ 93%). This finding nicely supports the steady-state absorption and emission peak assignments (Figure 1b,c), so the 510 nm excitation results in a closer SE intensity ratio in both solvents compared to 537 nm excitation. In other words, 510 nm excitation can pump both tautomers while being on resonance more with PS, leading to a more intense SE feature at ~555 nm (mainly assigned to the emission from PS). The redder 537 nm excitation primarily pumps PA, though by exciting the red tail of PS ground state (Figure 1b) a reduced SE peak intensity at ~555 nm is still visible.

The excitation wavelength dependence on the sub-ps decay magnitude of the 555 nm SE peak provides illuminating insights into the ESIPT reaction pathway. The EAS show that 510 nm excitation (Figure 4a,b) leads to a greater decay of the 555 nm SE peak on the sub-ps timescale (black→red) compared to 537 nm excitation (Figure 4c,d), especially in DCM. For a more quantitative verification, the magnitude of this sub-ps component can be obtained from Figure 3. In DCM and DMSO with 510 excitation, the amplitude weights for the sub-ps decay are 30% and 48%, respectively, much higher than the 537 nm excitation cases (15% and 31%). This process could be assigned to ESIPT originating from tautomer PS to either a transient state (where the proton is shared between adjacent carbonyl groups) or PA directly. Such an excitation-dependent change highlights intrinsic heterogeneity of the equilibrium chromophore population: besides pumping more PA ground-state population, a redder excitation pumps a redder PS ground state population that could be less prone to undergo ESIPT. This finding is based on the magnitude change of the sub-ps component for 555 nm SE peak (blue traces) assigned to PS during both excitations (i.e., 30%→15% in DCM, Figure 3a→c; 48%→31% in DMSO, Figure 3b→d).

Equilibrium and non-equilibrium inhomogeneous populations have been observed in a variety of systems;[100,101] for example, recent ultrafast spectroscopy of a methylated derivative of xylindein, dimethylxylindein, revealed a heterogeneous subpopulation that absorbs redder wavelengths and is more prone to intersystem crossing.[56]

Notably, the solvent appears to play a role in ESIPT process, since the blue SE at ~555 nm in DMSO consistently decays more on the sub-ps timescale than in DCM. This result suggests that DMSO facilitates proton transfer originating from PS species, likely due to stronger H-bonding interactions between the sulfoxide group (a proton acceptor) and hydroxy groups of the red pigment.[40,102] Whether this process involves a full ESIPT to form PA species (just being solvated by adjacent solvent molecules) or the proton partially transfers to form a transient state shared between the carbonyls and solvent molecule(s) can be further discussed in relation to several experimental results (see below).

In DCM, both excitations result in a minor rise of the redder SE peak at ~610 nm with a time constant of ~400 fs (Figure 3a,c). While this time constant is slightly faster than the 750 fs decay of the bluer SE peak, it can reasonably track the PS*→PA* transition via ESIPT (the asterisk denotes the excited state). As depicted by global analysis (Figure 4a,c black→red traces), this redder SE band red-shifts by ~9 nm in DCM on this timescale which is indicative of a slightly relaxed ESIPT product, PA*. This trend holds in DMSO as well with a slightly larger redshift of ~12 nm (Figure 4b,d black→red traces). Complementing this analysis, we observed a broad and weak SE feature above 700 nm that rises on a similar timescale for each of the respective experimental conditions (Figure S6). According to TD-DFT calculations (see Section 2.5), the transient state where a proton is shared between the adjacent carbonyl groups is predicted to emit at the reddest wavelengths (among all the calculated proton configurations, see Section 3.4 for details); therefore, the formation of this state where the proton may either proceed to form PA or return to PS occurs with a matching rise time constant. In essence, the apparent mismatch between the 400 fs rise component of 610 nm SE peak and 750 fs decay component of 555 nm SE peak, both in absolute value and amplitude weight, can be rationalized by the "two-way-street" between PS* and PA* species in the excited state, while the overall shift toward PA* can be confirmed by the only rise component retrieved from the 610 nm and >700 nm SE bands on a similar timescale as well as the population shift deduced from steady-state absorption to emission spectrum (Figure 1b→c). Furthermore, the lack of a ~400 fs rise of the 610 nm SE band in DMSO suggests that this solvent may inhibit a full transfer of the proton, in accord with the observed increase of PS* contribution to the steady-state emission spectrum of Draconin Red in DMSO (Figure S1).

Several useful connections can be drawn between the dynamics of blue and far-red SE band dynamics as follows. First, consistent with the sub-ps decay magnitude of the 555 nm SE peak, a bluer excitation results in a larger rise of the SE band above 700 nm with a similar time constant. For example, with 510 and 537 nm excitations of Draconin Red in DCM, the 555 nm SE peak decays on the sub-ps timescale with amplitude weights of 30% and 15%, respectively, while the far-red SE band rises with amplitude weights of 18% and 10%. This result shows a strikingly correlated nature to SE features separated by ~150–200 nm, due to the associated transient electronic states during initial ESIPT events induced by photoexcitation.[18] Second, upon comparison to the rise dynamics of this weak far-red SE feature in DMSO, a relatively larger ~750 fs rise constant is present upon both excitations, consistent with the more prominent ultrafast decay of the 555 nm SE peak on this timescale (blue traces in Figure 3b,d) versus DCM cases (blue traces in Figure 3a,c). In both solvents used, an interesting result about Draconin Red is that the ratio of the far-red SE rise magnitude over the 555 nm SE decay magnitude is close to $\frac{2}{3}$ (i.e., 18%:30%

and 10%:15% in DCM, 23%:48% and 22%:31% in DMSO), indicating an intrinsic molecular origin for the ESIPT reaction from PS* to PA* via an intermediate state (see Section 3.4).

The varying magnitudes of the ultrafast rise and decay components of the 555, 610, and >700 nm SE features are subject to spectral overlap and the associated transition oscillator strengths, yet collectively they suggest that not all the S_1 populations of Draconin Red can overcome the transition state energy barrier to complete the ESIPT reaction. The redshift of the ~555 nm SE peak (Figure 4) on the sub-ps timescale (black→red) reflects a portion of the chromophore population that cannot efficiently overcome this barrier, which is likely associated with a Draconin Red subpopulation that relaxes more in the same S_1 state without swift proton transfer, reminiscent of the redder PS population less prone to ESIPT upon 537 nm excitation. For corroboration, the EAS from global analysis for Draconin Red in DCM (Figure 4a vs. c) and DMSO (Figure 4b vs. d) conspicuously displays the red-shifted SE peak positions after excitation with a redder pump (537 nm), indicating that a different portion of the multidimensional PES is accessed.[17,18,65]

Interestingly, the redder SE peak also shows a minor ~750 fs decay (8%) upon 510 nm excitation in DMSO (Figures 3b and 4b). This result hints that bluer excitation of PA may excite the population to a higher-lying vibrational state that particularly facilitates ESIPT reaction in DMSO. By inspecting the OPA spectrum of PA (Figure 1b), the energetic difference between the reddest peak (~546 nm) and a bluer shoulder peak (~503 nm) is ~1570 cm^{-1}, indicative of a carbonyl group C=O and/or ring C=C stretching mode that is notably coupled to the electronic transition.[18,87] A plausible scenario is that upon excitation into a higher-lying vibrational state of PA with 510 nm pump, the Draconin Red C=O and C=C stretching motions become particularly active to enhance the ESIPT process; similar coherent mechanisms have been reported on organic chromophores via time-resolved fluorescence[48] and 2D-photon echo electronic spectroscopy.[103]

This analysis hints at a possible coherence between the "jiggling and wiggling" of atoms and the electronic change enabled by an ultrafast ESIPT reaction starting from PA* with excess energy by a bluer pump, and the apparent 750 fs time constant could have contributions from characteristic vibrational cooling,[18,29,62] which may result in better charge/energy transfer for optoelectronic applications in the redder-light-absorbing region (see Section 3.7).[5,6] An alternative interpretation could be that a sequential or concerted ESIDPT occurs on this timescale, which will be the subject of theoretical calculations as follows (e.g., PA*↔PS* occurs on the sub-ps timescale).

3.4. Computational Scans Yield Further Insights Into ESIPT Reaction. To delve deeper into the ESIPT reaction mechanism and transition state barriers, systematic calculations modeling the proton transfer in S_1 were performed.[69] Starting with PA form of Draconin Red, the two –OH bond distances in the molecular framework were scanned from ~1–2 Å (Section 2.5) resulting in a 2D-contour plot (Figure 5). In brief, TD-DFT optimizations of the chromophore in DCM were performed for ten steps with 0.1 Å step size, representing a "relaxed" scan as the molecular structure was optimized at each step with only the specific –OH bond distance fixed. There are two distinct –OH bond coordinates confirmed by 1D and 2D NMR:[50] $–OH_1$ (bottom, *ortho* to one of the methoxy groups) and $–OH_2$ (top, *meta* to the other methoxy group) as depicted for PA (state 1) in Figure 5 (bottom left corner). Due to symmetry of Draconin Red, states 2 and 3 are essentially identical and the energies of such ESIPT products (PS, since we started the computational scan from PA) are equivalent at a distance of ~1.6 Å irrespective of which proton ($–OH_1$, $–OH_2$) "jumps" to the adjacent carbonyl. Notably in PA, the starting distance for $–OH_1$ is 1.00919 Å while $–OH_2$ is 1.01444 Å. The corresponding distances (~1.004 and 1.009 Å) in PS are slightly different. Moreover, state 1 (gray) and transition state (black star) show slightly different values (transition state: $–OH_1$ = 1.20919 Å, $–OH_2$ = 1.21444 Å), but this difference may be affected by our scan step size of 0.1 Å. A finer step size could show some larger differences between these hydroxy bond distances due to asymmetry of the chromophore along vertical axis (Figure 5).

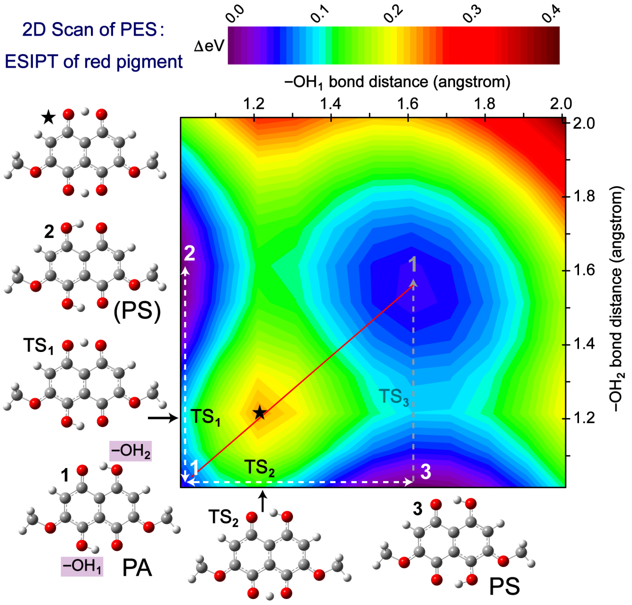

Figure 5. Potential energy surface of the relaxed S_1 state as a function of O–H bond distances. Chemical structures at the energy minima and saddle points are shown across corresponding axes for O–H_1 and O–H_2 bond distances as denoted by pink shades for PA tautomer (state 1), while the equivalent PS tautomers by symmetry (states 3 and 2) are depicted. White dashed double-headed arrows denote the reversible ESIPT via a single proton transfer through a small energy barrier transition state (TS_1 and TS_2), whereas the unlikely concerted double proton transfer is highlighted by the red line between state 1 (white) and 1 (gray, chemically equivalent by symmetry) via a high energy barrier marked by the black solid star (structure shown on the upper left corner).

While the final product states are equivalent, the routes to achieve these states are somewhat different as indicated by transition state 1 (TS_1) and TS_2. The transition state barrier for the –OH_2 coordinate is slightly lower (0.104 eV for TS_1) than the –OH_1 coordinate (0.137 eV for TS_2), suggesting that the former route is the main ESIPT coordinate observed during fs-TA experiments

(Figures 2–4). This transition state barrier difference may arise from the electron donating ability of the methoxy group, which can be considered as an *ortho*-directing activating group that donates electron density to the *ortho*-hydroxy group thus strengthening the $–OH_1$ bond (higher TS_2) and making ESIPT less feasible. In contrast, the methoxy group can also be considered as a *meta*-directing deactivating group that withdraws electron density from the *meta*-hydroxy group thus weakening the $–OH_2$ bond (lower TS_1) and making ESIPT more feasible. The resonance structures (Figure S2) indicate that the PA tautomer has more electron configurations in which a cationic $[=O^+–H]$ group is placed next to an anionic oxygen $–O^-$, poised to undergo keto-enol tautomerization through nucleophilic attack. Due to the placement of ketone and hydroxy groups in the PS tautomer, there are fewer ways for the molecule to be "primed" for ESIPT.

The calculations reveal that both the concerted and sequential DPT (see above) are unlikely in S_1. The concerted DPT transition state is highlighted by the star in Figure 5, where both protons are located in between the carbonyl groups. The energy for this transition state (0.239 eV) is more than double that of TS_1 and ~75% more than TS_2. For comparison, the sequential DPT is more energetically favorable than the concerted DPT by separating one high barrier into two smaller barriers; however, this route remains unlikely given that the $–OH_2$ ESIPT coordinate is more efficient, yet the subsequent transfer along the $–OH_1$ coordinate must overcome another relatively large transition barrier of 0.135 eV (see the green region between white state 2 and gray state 1 in Figure 5). Conversely, a sequential DPT could occur first by overcoming TS_2 energy barrier (0.137 eV), then overcoming TS_3 with a relatively low barrier of 0.107 eV (see the cyan region between state 3 and gray state 1 in Figure 5). Regardless of the actual route among those local energy extrema representing PA and PS, a DPT process beginning with PA (white state 1) would result in essentially the same tautomer (gray state 1, Figure 5), which represents a much less probable scenario both energetically and kinetically when compared to the ESIPT reaction with a single proton transfer between PA and PS tautomer states (see double-headed white arrows between states 1 and 2 or 3, Figure 5). Our calculations of the emission energy gaps of TS_1, TS_2, and the star in Figure 5 (ESIDPT) showed a general redshift from the PS (major) and PA (minor) species after electronic excitation, corroborating the observed far-red SE band dynamics (Figure S6) in close correlation with the PS* and PA* SE band intensity dynamics (Figure 3).

A rather surprising result emerged from the scans of ESIPT coordinates (Figure 5): the PA→PS tautomerization transition state barrier (state 1→2, 3) is significantly lower than the reverse process (states 3, 2→1). However, the fs-TA spectra reveal a clear ~750 fs decay of the 555 nm SE peak attributed to ESIPT from PS tautomer to TS_1 and/or TS_2, and PA tautomer. Why did the ultrafast measurements manifest an energetically unfavorable process instead of a more favorable pathway? We assert that the more downhill PA*→PS* process likely occurs within the cross-correlation of our optical spectroscopic setup (~120 fs) due to the reduced barrier height (see Section 3.5 below for more experimental support). It is thus reasonable to observe a relatively slow ESIPT process (~750 fs) due to its "bottleneck" effect as a rate-limiting step,[104] responsible for ~30% and 48% amplitude weights of the PS tautomer's SE peak decay after 510 nm excitation of Draconin Red in DCM and DMSO, respectively (Figure 3a,b). Furthermore, the observed higher fluorescence in the PS* emission region with 530 nm excitation vs. 500 nm excitation substantiates a favorable PA*→PS* conversion while PS*→PA* still occurs (Section 3.1). Faster ESIPT processes have been observed for similar organic chromophores including xylindein, alizarin, and indigo,[35,46,105] lending support to this interpretation. A series of temperature-dependent ultrafast measurements would allow for a calculation of activation energies using the Arrhenius equation, making it possible to better connect the PA*↔PS* transition state barriers with the ESIPT time constants.

3.5. FSRS Confirms Dominant PS Population in S$_0$ and Ultrafast ESIPT from PA*→PS*.

To shed further light on the ESIPT reaction coordinate beyond transient electronic spectroscopy like fs-TA, we implemented the tunable ground-state femtosecond stimulated Raman spectroscopy (GS-FSRS) with a series of Raman pump wavelengths to strategically enhance the vibrational signal from each tautomer species of Draconin Red in solution. On the basis of deconvoluted electronic absorption peaks (Figure 1b), a 530 nm Raman pump is more on resonance with PS (Figure 6a), whereas a 550 nm Raman pump has better resonance with PA (Figure 6b).

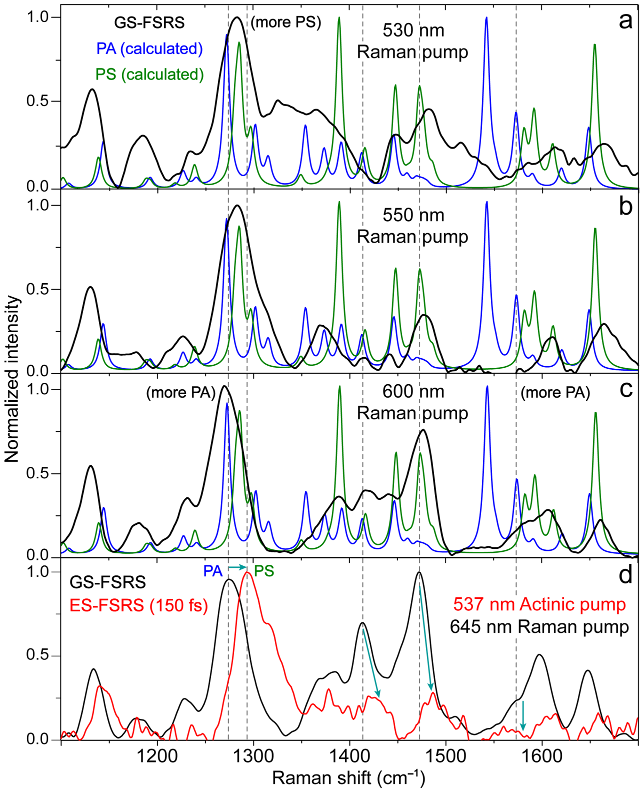

Figure 6. Ground-state (GS) and excited-state (ES)-FSRS on the red pigment with tunable laser pulses. GS-FSRS of Draconin Red in DCM using (a) 530 nm, (b) 550 nm, and (c) 600 nm Raman pumps (black) with a redder probe on the Stokes side, overlaid with the calculated spectrum for each tautomer (PA, blue; PS, green). (d) GS-FSRS (black) and ES-FSRS at 150 fs time delay after 537 nm excitation (red) obtained using 645 nm Raman pump and a bluer Raman probe on the anti-

Stokes side. Key Raman peaks for PA and PS tautomers are denoted by vertical gray dashed lines across the panels, and the light-induced ultrafast PA→PS transition is highlighted by four cyan arrows in panel d (e.g., a frequency blueshift <1300 cm^{-1}, and intensity drop of several modes between ~1400 and 1600 cm^{-1}).

During the FSRS experiments, a redder Raman pump at 600 nm can achieve a pre-resonance condition with PA (hence a purer PA spectrum) and exhibit a characteristic redshift of the most prominent mode (from ~1283 to 1270 cm^{-1}), consistent with the calculated trend from PS to PA spectra (green to blue traces in Figure 6a-c). The calculations were performed using the B3LYP functional and 6-311+G(3df,2p) basis set with implicit IEFPCM solvation in DCM as detailed in Section 2.6, resulting in Raman-active vibrational modes of each tautomer. The predicted spectra were scaled by a factor of 0.983 to match their experimental counterparts.[79,106] The overall decent match between the GS-FSRS and calculated PS spectrum supports a larger PS population (than PA) in S_0 at thermal equilibrium (see Section 3.1 above).

Notably, the ~1135 cm^{-1} mode in both tautomers consists of COH rocking motions of the hydroxy group at C8 (Figure 1a) with symmetric CC stretching between C8 and C1, which implies its relevance for proton transfer to the adjacent carbonyl group on C1.[41] A dominant ~1285 cm^{-1} mode consists of slightly different parts of the chromophore (skeletal motions) due to altered locations of the hydroxy groups relative to both sides of methoxy groups, and a substantial displacement vector of the COH rocking at C5 (PS) or C4 (PA). Moreover, in PS, the associated ring-breathing motion involves C5–OH and C8–OH stretching motions;[16,107] in PA, the associated asymmetric ring deformation involves C4–OH rocking motions. This difference in the 1285 cm^{-1} mode composition leads to a clear frequency blueshift of the calculated spectra from PA to PS in S_0 (Figure 6a-c), also reflected in the experimental spectra (e.g., more PA in Figure 6c vs. more

PS in Figure 6a). Moreover, the association with the C5 (PS) and C4 (PA) hydroxy rocking motions nicely corroborates the aforementioned ESIPT preference along the –OH_2 coordinate (Figure 5). The key evolution of GS→ES-FSRS peaks (black→red trace, Figure 6d) also substantiates an ultrafast PA*→PS* conversion, as the 537 nm actinic pump mainly excites PA species while the 645 nm Raman pump achieves a pre-resonance condition with both PA and PS species.[30,107] The PA* population rapidly tautomerizes to PS* (within 150 fs), signified by the marker band frequency blueshifts and intensity drops (highlighted by cyan arrows, Figure 6d).

Given the transient nature of proton motions and common challenges of observing exact proton locations with X-ray crystallography (a proton has no electron diffraction capability) or NMR spectroscopy on fs-to-ps timescales, detailed studies of organic chromophores like Draconin Red can provide new knowledge. Our implementation of a coherent nonlinear vibrational spectroscopy toolset like the wavelength-tunable FSRS with a ps-Raman-pump-fs-Raman-probe pair after an fs-actinic-pump for photoexcitation in the mixed time-frequency domain[18,30] allows crucial snapshots of initial structural dynamics starting from the onset of ESIPT reaction.[46,48] In particular, a combination of GS-FSRS on the Stokes side (Figure 6a-c) with ES-FSRS on the anti-Stokes side[29,30,56,108] (Figure 6d) using strategically chosen laser wavelengths guided by steady-state and time-resolved electronic spectral results (Figures 1–4) enables the elucidation of competing ESIPT pathways in S_1 of Draconin Red, signified by a much faster (<120 fs) PA*→PS* transition than the sub-ps (~750 fs) PS*→PA* transition as summarized below in Section 3.6. Both ESIPT time constants can be considered ultrafast, implying their intrinsically coherent nature involving anharmonic coupling between the actual proton transfer coordinate and other skeletal motions of the chromophore,[16,17,28] in accord with the observed ~20 cm^{-1} blueshift (1274→1294 cm^{-1}) of the rather global Raman marker band (C–O stretch and COH rock, see above). In other words, ultrafast electronic redistribution and proton motions work in tandem to shift the PA* and PS* population ratio within the first ps upon photoexcitation, and a more complete portrait can only be achieved by an integral spectroscopic characterization platform with fs-TA (Figures 2–4) and FSRS (Figure 6), aided by quantum calculations (Figure 5)[18,30] and steady-state spectroscopy (Figure 1), resulting in a unified PES model for Draconin Red in DCM (Figure 7) as detailed below.

3.6. Potential Energy Surface of the Red Pigment in Solution from Ground to Excited State. Using all the spectral data above with associated analysis and interpretations, we can sketch the PES involving S_0 and S_1 states of PA and PS tautomers (Figure 7). Upon 510 and 537 nm excitation of Draconin Red, both tautomers are primed to undergo an ultrafast (<120 fs) ESIPT reaction given similar energies of the unrelaxed excited states (PA*, PS*) and the much-reduced transition state barrier (compared to more relaxed states). With the cross-correlation of our optical setup on a similar timescale, we were unable to temporally resolve this process. The steady-state absorption and emission profiles (Figure 1b,c), in combination with fs-TA spectra (Figures 2–4, particularly the promptly emerged double-SE bands in the initial EAS as black traces in Figure 4), infer such an ESIPT event that occurs within the instrument response time. Though a dominant PS population is present at equilibrium, fs-TA spectra show that the 610 nm SE feature (assigned to PA*) is more intense around time zero (Figures 3 and 4). Even considering that the oscillator strength of PA* (~610 nm SE feature) is stronger than PS* from calculations (see Sections 2.5 and 3.1), this discrepancy can only be explained by an ultrafast PS*→PA* tautomerization.

Based on TD-DFT calculations, energy differences between the PA* and PA*' or PS* and PS*' states (the prime denotes a relaxed excited state) are ~253 or 282 meV, respectively, opening the door for ultrafast Franck-Condon relaxation. The difference between these calculated excited-state energy gaps is reflective of the different electronic structures of these two tautomers (see

Figure S2 for example). Similar to indigo, the molecular structure of Draconin Red is expected to be rigid, reflected by the mirror-like symmetry of the absorption and emission profiles, so such a swift relaxation out of the Franck-Condon region can be expected as an initial internal conversion toward the fluorescent state (denoted by PA*' and PS*' in Figure 7). This point is corroborated by the aforementioned energy gaps (<2300 cm^{-1}) corresponding to initial relaxation of PA* and PS*.

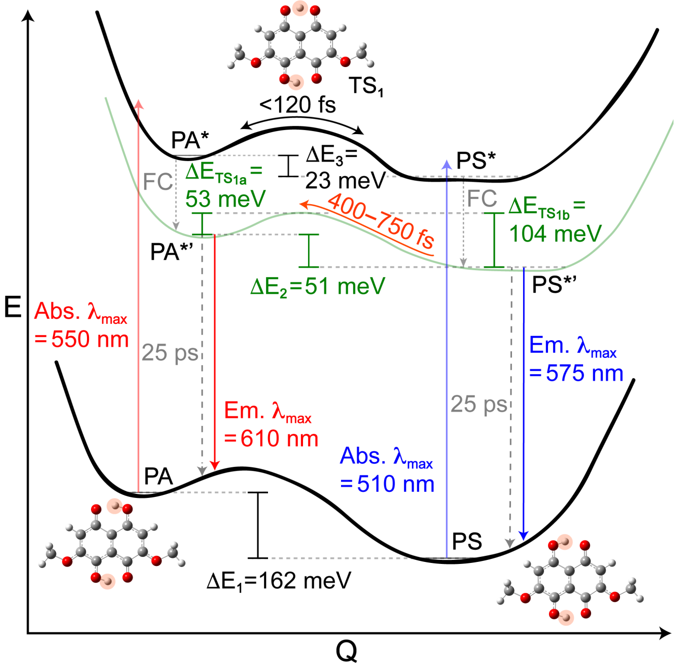

Figure 7. Potential energy surfaces (PESs) of the para-antisymmetric (PA) and para-symmetric (PS) tautomers of Draconin Red in DCM solution. ΔE_1, ΔE_2, and ΔE_3 represent the energy difference between two tautomers in the ground state (PA, PS), relaxed excited state (PA*', PS*'), and unrelaxed excited state (PA*, PS*), respectively. ΔE_{TS1a} / ΔE_{TS1b} represent the energy difference between PA*' / PS*' and the transition state barrier (TS_1). Gray dotted and dashed arrows represent Franck-Condon (FC) relaxation and rotation-assisted relaxation, respectively. The double-sided arrow depicts interconversion between PA* and PS* via ESIPT within the cross-correlation time, while orange arrow originating from PS*' denotes the slower ESIPT pathway. The insets show chemical structures of PA (lower left), PS (lower right), and the transition state

TS_1 (top middle). Steady-state absorption and emission wavelengths are shown for PA (red) and PS (blue) tautomers. Arrow lengths are not to scale (for illustration purpose only).

Afterwards, a rather unusual ESIPT process originating from the PS tautomer was observed with a 400–750 fs time constant. This characteristic timescale is relatively slow in comparison to many other ESIPT systems,[35,46,105] likely because the proton transfer from PS*' is an uphill process with a relatively large transition state barrier ($\Delta E_{TS1b} \approx$ 104 meV), while this ESIPT route remains competitive over other energy dissipation pathways (e.g., ~25 ps rotational motion that could be part of nonradiative relaxation, and fluorescence emission as radiative relaxation). Notably, our selective depiction of TS_1 energy barrier (Figure 7) stems from the TD-DFT-calculated $–OH_2$ vs. $–OH_1$ bond distance scanning results that reveal an intrinsic preference of TS_1 route with a smaller energy barrier to overcome for a single proton transfer (see Figure 5 in Section 3.4 above).

Furthermore, we comment on the observation of this sub-ps ESIPT time constant as follows. First, fs-TA spectra and the resulting dynamics demonstrate the net effect of ESIPT. That is to say, PA and PS tautomers are in a dynamic equilibrium interconverting between the two forms and transition states following electronic excitation. Second, PS is the dominant tautomer at thermal equilibrium (62–70%), hence the PS*'→PA*' tautomerization likely represents a large portion of the energy dissipation pathway. Third, the PA*→PS* conversion is a more downhill process with a reduced transition state barrier, therefore a majority of the PA ground-state population there is to begin with (30–38%) likely converts to PS* and PS*' within the instrument cross-correlation time. Following photoexcitation, the excited state is composed of the directly excited PS* population as well as ESIPT photoproduct PS* population, hence the observed higher fluorescence intensity within 560–590 nm after 530 nm excitation in DCM. In essence, with such a large PS population in S_0 and S_1, even if a small magnitude of PS* population tautomerized to PA*, it would be clearly observed on its intrinsic sub-ps timescale as the two tautomers interconvert in S_1.

3.7. Perspective on Optoelectronic and Photonic Applications of Draconin Red. Turning critical eyes to the future, there remains much to be studied to better understand the photoresponse of Draconin Red and evaluate its potential optoelectronic performance. The pigment forms needle-like crystals in solid state with notable inhomogeneity;[50] some orange-red crystals are essentially nonfluorescent while redder crystals display much enhanced fluorescence with waveguide-like properties (see right bottom panel in TOC graphic). Notably, the more needle-like red crystals exhibit peak fluorescence emission around 620 nm (close to SE peak wavelength of PA*' at ~615 nm in DCM and ~618 nm in DMSO, Figure 4), while the bulkier needle-like orange crystals exhibit a much broader fluorescence band extending to below 550 nm (compared to SE peak wavelength of PS*' at ~560 nm in DCM and ~565 nm in DMSO, Figure 4). Therefore, the different crystalline forms may be related to the two tautomers observed in solution and warrant further investigation. Preliminary experiments on Draconin Red in aqueous solution allowed the discovery of two red-shifted absorbing species which may represent the singly and doubly deprotonated species (Figure S7) that could provide additional insights regarding the energy dissipation pathways as well as emission red-shifting strategies. Our recent reports on xylindein and dimethylxylindein showed that H-bonding and ESIPT help to maintain the photostability of these photosensitive fungi-derived pigments.[35,37] Perhaps most importantly, there was evidence of possible coherence between certain vibrational motions and electronic transitions upon fs photoexcitation into the vibronic bands of these two tautomers of Draconin Red, primarily the redder-absorbing PA species (see Section 3.3 above). Future experiments with continued improvement of the optical setup to further temporally compress incident laser pulses may reveal detectable oscillations of the electronic signal coupled to impulsively excited skeletal motions.[17,18,28,30]

Furthermore, rigorous analysis of excitation-dependent ES-FSRS measurements may reveal additional "purely" vibrational coupling between low and high-frequency modes;[28] in particular, modes which involve the H-rocking of the specific hydroxy groups and C=O stretching of the carbonyls implicated to play pivotal roles during ESIPT.[46] The development of resonance Raman calculations paired with a multitude of Raman pump wavelength-dependent GS-FSFRS measurements may elucidate which vibrational modes are particularly coupled to certain electronic transitions of a particular conformational state.[78] Current challenges mainly lie in the compactness of Draconin Red since for optoelectronic applications, since a larger conjugated molecule is typically needed with a strong π-π overlap in the solid for efficient charge transport.[5] Nevertheless, the red pigment molecule serves as an important model system whose behavior in condensed phases can elucidate that of larger, more optoelectronically relevant chromophores.

With a bevy of equilibrium and non-equilibrium insights, an informed design of Draconin Red should be able to improve its functional properties and application potentials through strategic substitution(s) of the methoxy groups to stronger electron withdrawing/donating groups at opposite ends of the chromophore to incur more directionality of a CT state.[5,6] This engineering feat may enhance the intramolecular CT character of the pigment that is nearly ubiquitous for many high-performance optoelectronic molecules as we recently demonstrated for xylindein and its derivatives.[6,35,37,55,56] In particular, the exciton transport between chromophores with minimal energy loss (like in photosynthetic systems)[12,13] represents a crucial step to replicating and optimizing charge generation in designed organic electronics (e.g., donor-acceptor bulk heterojunction solar cells). However, the facile crystallization of Draconin Red from solution processing (Section 2.1) needs to be addressed before its effective use as a donor. In particular, the donor domain size must be comparable with the exciton diffusion length for the exciton to reach the donor/acceptor interface and subsequently separate into mobile charge carriers.[5]

Beyond a single Draconin Red molecule, when in solution aggregates, thin films or crystals,[50] the reduced distance between individual molecules could open new pathways for intermolecular H-bonding network and intermolecular charge transfer[35,37] and allow specific packing configurations (e.g., crystallization of Draconin Red into two polymorphs of different colors: red and orange) to modulate optical properties,[109] as well as the addition of secondary sensitizers that could acts as proton acceptors to the photoexcited PA* to further enhance and red-shift the radiative emission. We have collected the photoluminescence lifetime from Draconin Red in DCM solution and crystal forms (Figure S8) that well match the observed 690–840 ps decay time constants in DCM (Figure 3a,c) and the decreased values in solid state as expected.[37] Meanwhile, since we have a large PS population at thermal equilibrium (see Figure 1), the newly elucidated ultrafast ESIPT mechanisms between PS* and PA* (Figure 7) allow us to formulate an effective strategy in enhancing the PS*→PA* transition (states 2 or 3 to 1 in Figure 5) by reducing the excited-state transition state barrier (i.e., TS_1 and TS_2) through targeted molecular engineering.

Based on our discussions in Section 3.4, methoxy groups can be replaced by various electron-donating or withdrawing groups to fine-tune the hydroxy bond strength and ESIPT rate constant, depending on an intrinsic competition between the inequivalent $–OH_1$ and $–OH_2$ at *ortho*- and *meta*-sites to one of the methoxy groups, respectively. Conformational locking of one side or both sides of Draconin Red may offer opportunities for reducing ring deformations[35,107] and other nonradiative relaxation pathways and enhancing the FQY of PA*' (Figure 7) particularly after stabilization of the relaxed fluorescent state.[110,111] Besides the conformational polymorphism in close relationship to the intramolecular H-bonding network, we could further use molecular packing polymorphism (likely involving both intra- and intermolecular H-bonding)[112] as a beneficial strategy for device fabrication, improving the aforementioned waveguide properties of more efficiently, effectively prepared redder-absorbing-and-emitting crystals for potential applications in photonic circuits. Experiments on the crystalline red pigment samples are currently ongoing in our lab to better understand the variables (e.g., temperature, solvent, protonation state) involved during crystal growth to produce orange and red needle-like crystals with various packing configurations, compositions, disorders, and fluorescence quantum yields.

4. CONCLUSIONS

In summary, we have investigated the equilibrium properties of Draconin Red in solution via steady-state electronic spectroscopy, quantum calculations, and ground-state FSRS on the Stokes side (a redder Raman probe than Raman pump). To elucidate the non-equilibrium dynamics and photoresponse, we implemented both fs-TA spectroscopy and excited-state FSRS on the anti-Stokes side (a bluer Raman probe than Raman pump) and tracked ultrafast molecular behavior on the intrinsic timescales of electronic and atomic motions. To provide clarity on major tautomers present in solution at equilibrium, Franck-Condon Herzberg-Teller OPA/OPE calculations were performed to fit broad steady-state absorption/emission profiles arising from vibronic progression of two tautomers (PA, PS) due to different orientations of the hydroxy groups. Aside from determining that PS is the major conformation at equilibrium, this analysis helped to realize the full potential of excitation-dependent fs-TA measurements by aiding the assignment of major species being excited and transient species being formed in accord with the respective absorbing/emitting wavelengths. Notably, ultrafast electronic dynamics track the ESIPT reaction of photoexcited PS tautomer to an intermediate transition state where the proton is shared between the carbonyls as well as the formation of PA tautomer with a ~400–750 fs time constant in DCM and DMSO. Subsequently, the chromophore rotational relaxation occurs with shorter/longer time constants in DCM/DMSO, and this temporal component (impacted by solvent viscosity) preceding the apparent fluorescent lifetime approaches the ns timescale in DCM.

Upon comparison of Draconin Red in the two solvents studied, DMSO appears to facilitate the proton transfer as evidenced by a larger decay (rise) of the ~555 nm (far-red) SE features on the sub-ps timescale. This interesting result may be influenced by the H-bond donating/accepting strengths of the respective solvents. DCM cannot H-bond to the hydrogen/proton, so it does not affect the partial/full proton transfer to a large degree. Conversely, DMSO can H-bond to the hydrogen/proton through the sulfoxide group, hence it may enable initial proton transfer to a transition state yet inhibit full proton transfer to form PA. Surprisingly, scanning pertinent ESIPT coordinates in the excited state shows that PA*→PS* tautomerization should be more favorable while double ESIPT is highly unlikely. With limited evidence for PA*→PS* conversion from fs-TA experiments, it was speculated this process occurs within the instrument cross-correlation time, akin to many other ESIPT systems. Direct evidence of an ultrafast formation of PS* from PA* via ESIPT was revealed through ES-FSRS measurements after a 537 nm pump that primarily excites PA, with a 645 nm Raman pump pre-resonantly enhancing PA in the ground state, and a marker band at ~1274 cm^{-1} rapidly blue-shifts by ~20 cm^{-1} within 150 fs to form PS*. Finally, GS-FSRS with tunable resonance conditions substantiate the conclusion from steady-state spectroscopy and quantum calculations that PS is the dominant species in solution at equilibrium.

Besides obtaining fundamental knowledge from nonlinear coherent spectroscopy of Draconin Red as a potent ESIPT molecule from a wood fungus, we envision our detailed findings in this work to power future generations with a curious mind while enabling substantial progress and promoting collaboration in many areas including chemistry (physical, organic, analytical, green), physics, wood sciences, biomaterials, engineering, sustainable materials, and photosciences.

ASSOCIATED CONTENT

Supporting Information. The Supporting Information is available free of charge on the ACS Publications website at http://pubs.acs.org.

> Figures S1–S8 on steady-state spectra of Draconin Red in DMSO, resonance structures of two tautomers, calculated electronic absorption and emission (vibronic) spectra with default broadening parameters, FQY measurement of Draconin Red in various solvents, magic-angle TA measurement of Draconin Red in DCM after 510 nm excitation, far-red SE band (725–745 nm) dynamics, photobleaching data of Draconin Red in DCM and water, and photoluminescence lifetime measurements of Draconin Red in DCM and crystalline forms, additional references, the full authorship of Gaussian 09 and 16 software, and an Appendix with optimized structures and atomic coordinates of PA and PS tautomers (PDF)

AUTHOR INFORMATION

Corresponding Author

*E-mail: Chong.Fang@oregonstate.edu. Phone: 541-737-6704.

Notes

The authors declare no competing financial interests.

ACKNOWLEDGMENT

This work was supported by the U.S. National Science Foundation (NSF) grants CHE-2003550 to C.F. We appreciate the NSF MRI development grant (DMR-1920368) for additional personnel support. This research was also funded by the NSF "Energy for Sustainability" program (CBET-1705099). T.K. acknowledges the Oregon Lottery Graduate Scholarship at Oregon State University (2020–2021) and Milton Harris Graduate Fellowship at Department of Chemistry (Summer 2021). J.S. acknowledges the Oregon State University Provost's Distinguished Graduate Scholarship (2019–2020). We thank Dr. Cheng Chen for helpful discussions.

REFERENCES

(1) Pandey, L.; Risko, C.; Norton, J. E.; Brédas, J.-L. Donor–Acceptor Copolymers of Relevance for Organic Photovoltaics: A Theoretical Investigation of the Impact of Chemical Structure Modifications on the Electronic and Optical Properties. *Macromolecules* **2012**, *45*, 6405-6414.

(2) Bronstein, H.; Nielsen, C. B.; Schroeder, B. C.; McCulloch, I. The Role of Chemical Design in the Performance of Organic Semiconductors. *Nat. Rev. Chem.* **2020**, *4*, 66-77.

(3) Di Mauro, E.; Rho, D.; Santato, C. Biodegradation of Bio-Sourced and Synthetic Organic Electronic Materials towards Green Organic Electronics. *Nat. Commun.* **2021**, *12*, 3167.

(4) Budden, P. J.; Weiss, L. R.; Müller, M.; Panjwani, N. A.; Dowland, S.; Allardice, J. R.; Ganschow, M.; Freudenberg, J.; Behrends, J.; Bunz, U. H. F.; et al. Singlet Exciton Fission in a Modified Acene with Improved Stability and High Photoluminescence Yield. *Nat. Commun.* **2021**, *12*, 1527.

(5) Ostroverkhova, O. Organic Optoelectronic Materials: Mechanisms and Applications. *Chem. Rev.* **2016**, *116*, 13279-13412.

(6) Krueger, T. D.; Fang, C. Elucidating Inner Workings of Naturally Sourced Organic Optoelectronic Materials with Ultrafast Spectroscopy. *Chem. Eur. J.* **2021**, in press. DOI: 10.1002/chem.202102766.

(7) Dean, J. C.; Mirkovic, T.; Toa, Z. S. D.; Oblinsky, D. G.; Scholes, G. D. Vibronic Enhancement of Algae Light Harvesting. *Chem* **2016**, *1*, 858-872.

(8) Piatkowski, L.; Accanto, N.; van Hulst, N. F. Ultrafast Meets Ultrasmall: Controlling Nanoantennas and Molecules. *ACS Photonics* **2016**, *3*, 1401-1414.

(9) Pradhan, S.; Brooks, A. K.; Yadavalli, V. K. Nature-Derived Materials for the Fabrication of Functional Biodevices. *Mater. Today Bio* **2020**, *7*, 100065.

(10) Scholes, G. D.; Rumbles, G. Excitons in nanoscale systems. *Nat. Mater.* **2006**, *5*, 683-696.

(11) Berera, R.; van Grondelle, R.; Kennis, J. M. Ultrafast Transient Absorption Spectroscopy: Principles and Application to Photosynthetic Systems. *Photosynth. Res.* **2009**, *101*, 105-118.

(12) Mirkovic, T.; Ostroumov, E. E.; Anna, J. M.; van Grondelle, R.; Govindjee; Scholes, G. D. Light Absorption and Energy Transfer in the Antenna Complexes of Photosynthetic Organisms. *Chem. Rev.* **2017**, *117*, 249-293.

(13) Scholes, G. D.; Fleming, G. R.; Chen, L. X.; Aspuru-Guzik, A.; Buchleitner, A.; Coker, D. F.; Engel, G. S.; van Grondelle, R.; Ishizaki, A.; Jonas, D. M.; et al. Using Coherence to Enhance Function in Chemical and Biophysical Systems. *Nature* **2017**, *543*, 647-656.

(14) Rathbone, H. W.; Davis, J. A.; Michie, K. A.; Goodchild, S. C.; Robertson, N. O.; Curmi, P. M. G. Coherent Phenomena in Photosynthetic Light Harvesting: Part One—Theory and Spectroscopy. *Biophys. Rev.* **2018**, *10*, 1427-1441.

(15) Rathbone, H. W.; Davis, J. A.; Michie, K. A.; Goodchild, S. C.; Robertson, N. O.; Curmi, P. M. G. Coherent Phenomena in Photosynthetic Light Harvesting: Part Two—Observations in Biological Systems. *Biophys. Rev.* **2018**, *10*, 1443-1463.

(16) Fang, C.; Frontiera, R. R.; Tran, R.; Mathies, R. A. Mapping GFP Structure Evolution During Proton Transfer with Femtosecond Raman Spectroscopy. *Nature* **2009**, *462*, 200-204.

(17) Hoffman, D. P.; Mathies, R. A. Femtosecond Stimulated Raman Exposes the Role of Vibrational Coherence in Condensed-Phase Photoreactivity. *Acc. Chem. Res.* **2016**, *49*, 616-625.

(18) Fang, C.; Tang, L.; Chen, C. Unveiling Coupled Electronic and Vibrational Motions of Chromophores in Condensed Phases. *J. Chem. Phys.* **2019**, *151*, 200901.

(19) Agmon, N.; Huppert, D.; Masad, A.; Pines, E. Excited-State Proton-Transfer to Methanol Water Mixtures. *J. Phys. Chem.* **1991**, *95*, 10407-10413.

(20) Tran-Thi, T.-H.; Gustavsson, T.; Prayer, C.; Pommeret, S.; Hynes, J. T. Primary Ultrafast Events Preceding the Photoinduced Proton Transfer from Pyranine to Water. *Chem. Phys. Lett.* **2000**, *329*, 421-430.

(21) Rini, M.; Magnes, B.-Z.; Pines, E.; Nibbering, E. T. J. Real-Time Observation of Bimodal Proton Transfer in Acid-Base Pairs in Water. *Science* **2003**, *301*, 349-352.

(22) Mohammed, O. F.; Pines, D.; Dreyer, J.; Pines, E.; Nibbering, E. T. J. Sequential Proton Transfer through Water Bridges in Acid-Base Reactions. *Science* **2005**, *310*, 83-86.

(23) Nibbering, E. T. J.; Fidder, H.; Pines, E. Ultrafast Chemistry: Using Time-Resolved Vibrational Spectroscopy for Interrogation of Structural Dynamics. *Annu. Rev. Phys. Chem.* **2005**, *56*, 337-367.

(24) Hynes, J. T. Physical Chemistry: The Peripatetic proton. *Nature* **2007**, *446*, 270-273.

(25) Liu, W.; Han, F.; Smith, C.; Fang, C. Ultrafast Conformational Dynamics of Pyranine during Excited State Proton Transfer in Aqueous Solution Revealed by Femtosecond Stimulated Raman Spectroscopy. *J. Phys. Chem. B* **2012**, *116*, 10535-10550.

(26) Han, F.; Liu, W.; Fang, C. Excited-State Proton Transfer of Photoexcited Pyranine in Water Observed by Femtosecond Stimulated Raman Spectroscopy. *Chem. Phys.* **2013**, *422*, 204-219.

(27) Simkovitch, R.; Shomer, S.; Gepshtein, R.; Huppert, D. How Fast Can a Proton-Transfer Reaction Be Beyond the Solvent-Control Limit? *J. Phys. Chem. B* **2015**, *119*, 2253-2262.

(28) Liu, W.; Wang, Y.; Tang, L.; Oscar, B. G.; Zhu, L.; Fang, C. Panoramic Portrait of Primary Molecular Events Preceding Excited State Proton Transfer in Water. *Chem. Sci.* **2016**, *7*, 5484-5494.

(29) Liu, W.; Tang, L.; Oscar, B. G.; Wang, Y.; Chen, C.; Fang, C. Tracking Ultrafast Vibrational Cooling During Excited State Proton Transfer Reaction with Anti-Stokes and Stokes Femtosecond Stimulated Raman Spectroscopy. *J. Phys. Chem. Lett.* **2017**, *8*, 997–1003.

(30) Fang, C.; Tang, L.; Oscar, B. G.; Chen, C. Capturing Structural Snapshots during Photochemical Reactions with Ultrafast Raman Spectroscopy: From Materials Transformation to Biosensor Responses. *J. Phys. Chem. Lett.* **2018**, *9*, 3253–3263.

(31) Flom, S. R.; Barbara, P. F. Proton Transfer and Hydrogen Bonding in the Internal Conversion of S_1 Anthraquinones. *J. Phys. Chem.* **1985**, *89*, 4489-4494.

(32) Lochbrunner, S.; Wurzer, A. J.; Riedle, E. Microscopic Mechanism of Ultrafast Excited-State Intramolecular Proton Transfer: A 30-fs Study of 2-(2'-Hydroxyphenyl)benzothiazole. *J. Phys. Chem. A* **2003**, *107*, 10580-10590.

(33) Chen, K.-Y.; Cheng, Y.-M.; Lai, C.-H.; Hsu, C.-C.; Ho, M.-L.; Lee, G.-H.; Chou, P.-T. Ortho Green Fluorescence Protein Synthetic Chromophore; Excited-State Intramolecular Proton Transfer via a Seven-Membered-Ring Hydrogen-Bonding System. *J. Am. Chem. Soc.* **2007**, *129*, 4534-4535.

(34) Zhou, P.; Han, K. Unraveling the Detailed Mechanism of Excited-State Proton Transfer. *Acc. Chem. Res.* **2018**, *51*, 1681-1690.

(35) Krueger, T. D.; Giesbers, G.; Van Court, R. C.; Zhu, L.; Kim, R.; Beaudry, C. M.; Robinson, S. C.; Ostroverkhova, O.; Fang, C. Ultrafast Dynamics and Photoresponse of a Fungi-Derived Pigment Xylindein from Solution to Thin Films. *Chem. Eur. J.* **2021**, *27*, 5627-5631.

(36) Wu, J.-J.; Gao, H.; Lai, R.; Zhuo, M.-P.; Feng, J.; Wang, X.-D.; Wu, Y.; Liao, L.-S.; Jiang, L. Near-Infrared Organic Single-Crystal Nanolaser Arrays Activated by Excited-State Intramolecular Proton Transfer. *Matter* **2020**, *2*, 1233-1243.

(37) Giesbers, G.; Krueger, T. D.; Van Schenck, J. D. B.; Kim, R.; Van Court, R. C.; Robinson, S. C.; Beaudry, C. M.; Fang, C.; Ostroverkhova, O. Role of Hydroxyl Groups in the Photophysics, Photostability, and (Opto)electronic Properties of the Fungi-Derived Pigment Xylindein. *J. Phys. Chem. C* **2021**, *125*, 6534–6545.

(38) Zhao, J.; Ji, S.; Chen, Y.; Guo, H.; Yang, P. Excited State Intramolecular Proton Transfer (ESIPT): From Principal Photophysics to the Development of New Chromophores and Applications in Fluorescent Molecular Probes and Luminescent Materials. *Phys. Chem. Chem. Phys.* **2012**, *14*, 8803-8817.

(39) Padalkar, V. S.; Seki, S. Excited-State Intramolecular Proton-Transfer (ESIPT)-Inspired Solid State Emitters. *Chem. Soc. Rev.* **2016**, *45*, 169-202.

(40) Ameer-Beg, S.; Ormson, S. M.; Brown, R. G.; Matousek, P.; Towrie, M.; Nibbering, E. T. J.; Foggi, P.; Neuwahl, F. V. R. Ultrafast Measurements of Excited State Intramolecular Proton Transfer (ESIPT) in Room Temperature Solutions of 3-Hydroxyflavone and Derivatives. *J. Phys. Chem. A* **2001**, *105*, 3709-3718.

(41) Lochbrunner, S.; Szeghalmi, A.; Stock, K.; Schmitt, M. Ultrafast Proton Transfer of 1-Hydroxy-2-Acetonaphthone: Reaction Path from Resonance Raman and Transient Absorption Studies. *J. Chem. Phys.* **2005**, *122*, 244315.

(42) Ma, J.; Zhao, J.; Yang, P.; Huang, D.; Zhang, C.; Li, Q. New Excited State Intramolecular Proton Transfer (ESIPT) Dyes based on Naphthalimide and Observation of Long-Lived Triplet Excited States. *Chem. Commun.* **2012**, *48*, 9720-9722.

(43) Matylitsky, V. V.; Lenz, M. O.; Wachtveitl, J. Observation of pH-Dependent Back-Electron-Transfer Dynamics in Alizarin/TiO_2 Adsorbates: Importance of Trap States. *J. Phys. Chem. B* **2006**, *110*, 8372-8379.

(44) Kaniyankandy, S.; Verma, S.; Mondal, J. A.; Palit, D. K.; Ghosh, H. N. Evidence of Multiple Electron Injection and Slow Back Electron Transfer in Alizarin-Sensitized Ultrasmall TiO_2 Particles. *J. Phys. Chem. C* **2009**, *113*, 3593-3599.

(45) Mech, J.; Grela, M. A.; Szaciłowski, K. Ground and Excited State Properties of Alizarin and Its Isomers. *Dyes Pigm.* **2014**, *103*, 202-213.

(46) Jen, M.; Lee, S.; Jeon, K.; Hussain, S.; Pang, Y. Ultrafast Intramolecular Proton Transfer of Alizarin Investigated by Femtosecond Stimulated Raman Spectroscopy. *J. Phys. Chem. B* **2017**, *121*, 4129-4136.

(47) Berenbeim, J. A.; Boldissar, S.; Owens, S.; Haggmark, M. R.; Gate, G.; Siouri, F. M.; Cohen, T.; Rode, M. F.; Patterson, C. S.; de Vries, M. S. Excited State Intramolecular Proton

Transfer in Hydroxyanthraquinones: Toward Predicting Fading of Organic Red Colorants in Art. *Sci. Adv.* **2019**, *5*, eaaw5227.

(48) Kim, C. H.; Joo, T. Coherent Excited State Intramolecular Proton Transfer Probed by Time-Resolved Fluorescence. *Phys. Chem. Chem. Phys.* **2009**, *11*, 10266-10269.

(49) Weber, G.; Chen, H.-L.; Hinsch, E.; Freitas, S.; Robinson, S. Pigments Extracted from the Wood-Staining Fungi *Chlorociboria aeruginosa*, *Scytalidium cuboideum*, and *S. ganodermophthorum* Show Potential for Use as Textile Dyes. *Coloration Technol.* **2014**, *130*, 445-452.

(50) Vega Gutierrez, S. M.; Hazell, K. K.; Simonsen, J.; Robinson, S. C. Description of a Naphthoquinonic Crystal Produced by the Fungus *Scytalidium cuboideum*. *Molecules* **2018**, *23*, 1905.

(51) Chang, C. W. J.; Moore, R. E.; Scheuer, P. J. The Structure of Spinochrome M. *J. Am. Chem. Soc.* **1964**, *86*, 2959-2961.

(52) McGovern, E. P.; Bentley, R. Biosynthesis of Flaviolin and 5,8-Dihydroxy-2,7-Dimethoxy-1,4-Naphthoquinone. *Biochemistry* **1975**, *14*, 3138-3143.

(53) Gerber, N. N.; Wieclawek, B. The Structures of Two Naphthoquinone Pigments from an Actinomycete. *J. Org. Chem.* **1966**, *31*, 1496-1498.

(54) Giesbers, G.; Van Schenck, J.; Vega Gutierrez, S.; Robinson, S.; Ostroverkhova, O. Fungi-Derived Pigments for Sustainable Organic (Opto)Electronics. *MRS Adv.* **2018**, *3*, 3459-3464.

(55) Giesbers, G.; Van Schenck, J.; Quinn, A.; Van Court, R.; Vega Gutierrez, S. M.; Robinson, S. C.; Ostroverkhova, O. Xylindein: Naturally Produced Fungal Compound for Sustainable (Opto)electronics. *ACS Omega* **2019**, *4*, 13309-13318.

(56) Krueger, T. D.; Tang, L.; Giesbers, G.; Van Court, R. C.; Zhu, L.; Robinson, S. C.; Ostroverkhova, O.; Fang, C. Ultrafast Triplet State Formation in a Methylated Fungi-Derived Pigment: Toward Rational Molecular Design for Sustainable Optoelectronics. *J. Phys. Chem. C* **2021**, *125*, 17565–17572.

(57) Kumpulainen, T.; Lang, B.; Rosspeintner, A.; Vauthey, E. Ultrafast Elementary Photochemical Processes of Organic Molecules in Liquid Solution. *Chem. Rev.* **2017**, *117*, 10826-10939.

(58) Vega Gutierrez, S. M.; Van Court, R. C.; Stone, D. W.; Konkler, M. J.; Groth, E. N.; Robinson, S. C. Relationship between Molarity and Color in the Crystal ('Dramada') Produced by *Scytalidium cuboideum*, in Two Solvents. *Molecules* **2018**, *23*, 2581.

(59) Vega Gutierrez, S. M.; He, Y.; Cao, Y.; Stone, D.; Walsh, Z.; Malhotra, R.; Chen, H.-L.; Chang, C.-H.; Robinson, S. C. Feasibility and Surface Evaluation of the Pigment from *Scytalidium cuboideum* for Inkjet Printing on Textiles. *Coatings* **2019**, *9*, 266.

(60) Robinson, S. C.; Tudor, D.; Snider, H.; Cooper, P. A. Stimulating Growth and Xylindein Production of *Chlorociboria aeruginascens* in Agar-Based Systems. *AMB Expr.* **2012**, *2*, 15.

(61) Fonin, A. V.; Sulatskaya, A. I.; Kuznetsova, I. M.; Turoverov, K. K. Fluorescence of Dyes in Solutions with High Absorbance. Inner Filter Effect Correction. *PLOS ONE* **2014**, *9*, e103878.

(62) Krueger, T. D.; Boulanger, S. A.; Zhu, L.; Tang, L.; Fang, C. Discovering a Rotational Barrier within a Charge-Transfer State of a Photoexcited Chromophore in Solution. *Struct. Dyn.* **2020**, *7*, 024901.

(63) Rurack, K.; Spieles, M. Fluorescence Quantum Yields of a Series of Red and Near-Infrared Dyes Emitting at 600−1000 nm. *Anal. Chem.* **2011**, *83*, 1232-1242.

(64) Zhu, L.; Liu, W.; Fang, C. A Versatile Femtosecond Stimulated Raman Spectroscopy Setup with Tunable Pulses in the Visible to Near Infrared. *Appl. Phys. Lett.* **2014**, *105*, 041106.

(65) Tang, L.; Zhu, L.; Taylor, M. A.; Wang, Y.; Remington, S. J.; Fang, C. Excited State Structural Evolution of a GFP Single-Site Mutant Tracked by Tunable Femtosecond-Stimulated Raman Spectroscopy. *Molecules* **2018**, *23*, 2226.

(66) Chen, C.; Zhu, L.; Fang, C. Femtosecond Stimulated Raman Line Shapes: Dependence on Resonance Conditions of Pump and Probe Pulses. *Chin. J. Chem. Phys.* **2018**, *31*, 492-502.

(67) Frisch, M. J.; Trucks, G. W.; Schlegel, H. B.; Scuseria, G. E.; Robb, M. A.; Cheeseman, J. R.; Scalmani, G.; Barone, V.; Mennucci, B.; Petersson, G. A.; et al. *Gaussian 09, revision B.1*; Gaussian, Inc.: Wallingford, CT, 2009.

(68) Frisch, M. J.; Trucks, G. W.; Schlegel, H. B.; Scuseria, G. E.; Robb, M. A.; Cheeseman, J. R.; Scalmani, G.; Barone, V.; Petersson, G. A.; Nakatsuji, H.; et al. *Gaussian 16, revision A.03*; Gaussian, Inc.: Wallingford, CT, 2016.

(69) Zhao, J.; Dong, H.; Zheng, Y. Theoretical Insights Into the Excited State Double Proton Transfer Mechanism of Deep Red Pigment Alkannin. *J. Phys. Chem. A* **2018**, *122*, 1200-1208.

(70) Kamlet, M. J.; Abboud, J.-L. M.; Abraham, M. H.; Taft, R. W. Linear Solvation Energy Relationships. 23. A Comprehensive Collection of the Solvatochromic Parameters, π*, α, and β, and Some Methods for Simplifying the Generalized Solvatochromic Equation. *J. Org. Chem.* **1983**, *48*, 2877-2887.

(71) Reichardt, C. Solvatochromic Dyes as Solvent Polarity Indicators. *Chem. Rev.* **1994**, *94*, 2319-2358.

(72) Solntsev, K. M.; Huppert, D.; Tolbert, L. M.; Agmon, N. Solvatochromic Shifts of "Super" Photoacids. *J. Am. Chem. Soc.* **1998**, *120*, 7981-7982.

(73) Klymchenko, A. S. Solvatochromic and Fluorogenic Dyes as Environment-Sensitive Probes: Design and Biological Applications. *Acc. Chem. Res.* **2017**, *50*, 366-375.

(74) Chen, C.; Boulanger, S. A.; Sokolov, A. I.; Baranov, M. S.; Fang, C. A Novel Dialkylamino GFP Chromophore as an Environment-Polarity Sensor Reveals the Role of Twisted Intramolecular Charge Transfer. *Chemosensors* **2021**, *9*, 234.

(75) Chen, C.; Baranov, M. S.; Zhu, L.; Baleeva, N. S.; Smirnov, A. Y.; Zaitseva, S.; Yampolsky, I. V.; Solntsev, K. M.; Fang, C. Designing Redder and Brighter Fluorophores by Synergistic Tuning of Ground and Excited States. *Chem. Commun.* **2019**, *55*, 2537-2540.

(76) Gai, F.; Fehr, M. J.; Petrich, J. W. Observation of Excited-State Tautomerization in the Antiviral Agent Hypericin and Identification of Its Fluorescent Species. *J. Phys. Chem.* **1994**, *98*, 5784-5795.

(77) Le Person, A.; Cornard, J.-P.; Say-Liang-Fat, S. Studies of the Tautomeric Forms of Alizarin in the Ground State by Electronic Spectroscopy Combined with Quantum Chemical Calculations. *Chem. Phys. Lett.* **2011**, *517*, 41-45.

(78) Spillane, K. M.; Dasgupta, J.; Lagarias, J. C.; Mathies, R. A. Homogeneity of Phytochrome Cph1 Vibronic Absorption Revealed by Resonance Raman Intensity Analysis. *J. Am. Chem. Soc.* **2009**, *131*, 13946-13948.

(79) Taylor, M. A.; Zhu, L.; Rozanov, N. D.; Stout, K. T.; Chen, C.; Fang, C. Delayed Vibrational Modulation of the Solvated GFP Chromophore into a Conical Intersection. *Phys. Chem. Chem. Phys.* **2019**, *21*, 9728-9739.

(80) Dierksen, M.; Grimme, S. Density Functional Calculations of the Vibronic Structure of Electronic Absorption Spectra. *J. Chem. Phys.* **2004**, *120*, 3544-3554.

(81) Adamo, C.; Jacquemin, D. The Calculations of Excited-State Properties with Time-Dependent Density Functional Theory. *Chem. Soc. Rev.* **2013**, *42*, 845-856.

(82) Zuehlsdorff, T. J.; Montoya-Castillo, A.; Napoli, J. A.; Markland, T. E.; Isborn, C. M. Optical Spectra in the Condensed Phase: Capturing Anharmonic and Vibronic Features using Dynamic and Static Approaches. *J. Chem. Phys.* **2019**, *151*, 074111.

(83) Zuehlsdorff, T. J.; Shedge, S. V.; Lu, S.-Y.; Hong, H.; Aguirre, V. P.; Shi, L.; Isborn, C. M. Vibronic and Environmental Effects in Simulations of Optical Spectroscopy. *Annu. Rev. Phys. Chem.* **2021**, *72*, 165-188.

(84) Bloino, J.; Biczysko, M.; Santoro, F.; Barone, V. General Approach to Compute Vibrationally Resolved One-Photon Electronic Spectra. *J. Chem. Theory Comput.* **2010**, *6*, 1256-1274.

(85) Chen, F.; Zhao, X.; Liang, W. One- and Two-Photon Absorption Spectra of the Yellow Fluorescent Protein Citrine: Effects of Intramolecular Electron-Vibrational Coupling and Intermolecular Interactions. *Mol. Phys.* **2018**, *116*, 885-897.

(86) Benkyi, I.; Tapavicza, E.; Fliegl, H.; Sundholm, D. Calculation of Vibrationally Resolved Absorption Spectra of Acenes and Pyrene. *Phys. Chem. Chem. Phys.* **2019**, *21*, 21094-21103.

(87) Tachibana, S. R.; Tang, L.; Zhu, L.; Liu, W.; Wang, Y.; Fang, C. Watching an Engineered Calcium Biosensor Glow: Altered Reaction Pathways before Emission. *J. Phys. Chem. B* **2018**, *122*, 11986–11995.

(88) Maroncelli, M.; Fleming, G. R. Picosecond Solvation Dynamics of Coumarin 153: The Importance of Molecular Aspects of Solvation. *J. Chem. Phys.* **1987**, *86*, 6221-6239.

(89) Chen, C.; Zhu, L.; Baranov, M. S.; Tang, L.; Baleeva, N. S.; Smirnov, A. Y.; Yampolsky, I. V.; Solntsev, K. M.; Fang, C. Photoinduced Proton Transfer of GFP-Inspired Fluorescent Superphotoacids: Principles and Design. *J. Phys. Chem. B* **2019**, *123*, 3804-3821.

(90) Lawler, C.; Fayer, M. D. Proton Transfer in Ionic and Neutral Reverse Micelles. *J. Phys. Chem. B* **2015**, *119*, 6024-6034.

(91) Simkovitch, R.; Rozenman, G. G.; Huppert, D. A Fresh Look into the Time-Resolved Fluorescence of 8-Hydroxy-1,3,6-Pyrenetrisulfonate with the Use of the Fluorescence Up-Conversion Ttechnique. *J. Photochem. Photobiol. A: Chemistry* **2017**, *344*, 15-27.

(92) Jiang, B.; Aliyan, A.; Cook, N. P.; Augustine, A.; Bhak, G.; Maldonado, R.; Smith McWilliams, A. D.; Flores, E. M.; Mendez, N.; Shahnawaz, M.; et al. Monitoring the Formation of Amyloid Oligomers Using Photoluminescence Anisotropy. *J. Am. Chem. Soc.* **2019**, *141*, 15605-15610.

(93) Oscar, B. G.; Liu, W.; Rozanov, N. D.; Fang, C. Ultrafast Intermolecular Proton Transfer to a Proton Scavenger in an Organic Solvent. *Phys. Chem. Chem. Phys.* **2016**, *18*, 26151-26160.

(94) Horng, M. L.; Gardecki, J. A.; Papazyan, A.; Maroncelli, M. Subpicosecond Measurements of Polar Solvation Dynamics: Coumarin 153 Revisited. *J. Phys. Chem.* **1995**, *99*, 17311-17337.

(95) Chen, C.; Tachibana, S. R.; Baleeva, N. S.; Myasnyanko, I. N.; Bogdanov, A. M.; Gavrikov, A. S.; Mishin, A. S.; Malyshevskaya, K. K.; Baranov, M. S.; Fang, C. Developing Bright Green Fluorescent Protein (GFP)-like Fluorogens for Live-Cell Imaging with Nonpolar Protein−Chromophore Interactions. *Chem. Eur. J.* **2021**, *27*, 8946-8950.

(96) Tamuly, C.; Barooah, N.; Laskar, M.; Sarma, R. J.; Baruah, J. B. Fluorescence Quenching and Enhancement by H-bonding Interactions in Some Nitrogen Containing Fluorophores. *Supramol. Chem.* **2006**, *18*, 605-613.

(97) Yang, J.-S.; Huang, G.-J.; Liu, Y.-H.; Peng, S.-M. Photoisomerization of the Green Fluorescence Protein Chromophore and the *meta*- and *para*-Amino Analogues. *Chem. Commun.* **2008**, *2008*, 1344-1346.

(98) Hossen, T.; Sahu, K. New Insights on Hydrogen-Bond-Induced Fluorescence Quenching Mechanism of C102–Phenol Complex via Proton Coupled Electron Transfer. *J. Phys. Chem. A* **2018**, *122*, 2394-2400.

(99) Snellenburg, J. J.; Laptenok, S. P.; Seger, R.; Mullen, K. M.; van Stokkum, I. H. M. Glotaran: A Java-Based Graphical User Interface for the R-Package TIMP. *J. Stat. Softw.* **2012**, *49*, 1-22.

(100) Krueger, T. D.; Tang, L.; Zhu, L.; Breen, I. L.; Wachter, R. M.; Fang, C. Dual Illumination Enhances Transformation of an Engineered Green-to-Red Photoconvertible Fluorescent Protein. *Angew. Chem. Int. Ed.* **2020**, *59*, 1644-1652.

(101) Tachibana, S. R.; Tang, L.; Zhu, L.; Takeda, Y.; Fushimi, K.; Ueda, Y.; Nakajima, T.; Kuwasaki, Y.; Sato, M.; Narikawa, R.; Fang, C. An Engineered Biliverdin-Compatible Cyanobacteriochrome Enables a Unique Ultrafast Reversible Photoswitching Pathway. *Int. J. Mol. Sci.* **2021**, *22*, 5252.

(102) Jen, M.; Jeon, K.; Lee, S.; Hwang, S.; Chung, W.-j.; Pang, Y. Ultrafast Intramolecular Proton Transfer Reactions and Solvation Dynamics of DMSO. *Struct. Dyn.* **2019**, *6*, 064901.

(103) Johnson, P. J. M.; Farag, M. H.; Halpin, A.; Morizumi, T.; Prokhorenko, V. I.; Knoester, J.; Jansen, T. L. C.; Ernst, O. P.; Miller, R. J. D. The Primary Photochemistry of Vision Occurs at the Molecular Speed Limit. *J. Phys. Chem. B* **2017**, *121*, 4040-4047.

(104) Hong, M. J.; Zhu, L.; Chen, C.; Tang, L.; Lin, Y.-H.; Li, W.; Johnson, R.; Chattopadhyay, S.; Snaith, H. J.; Fang, C.; et al. Time-Resolved Changes in Dielectric Constant of Metal Halide Perovskites under Illumination. *J. Am. Chem. Soc.* **2020**, *142*, 19799-19803.

(105) He, X.; Yang, F.; Li, S.; He, X.; Yu, A.; Chen, J.; Xu, J.; Wang, J. Ultrafast Excited-State Intermolecular Proton Transfer in Indigo Oligomer. *J. Phys. Chem. A* **2019**, *123*, 6463-6471.

(106) Merrick, J. P.; Moran, D.; Radom, L. An Evaluation of Harmonic Vibrational Frequency Scale Factors. *J. Phys. Chem. A* **2007**, *111*, 11683-11700.

(107) Fang, C.; Tang, L. Mapping Structural Dynamics of Proteins with Femtosecond Stimulated Raman Spectroscopy. *Annu. Rev. Phys. Chem.* **2020**, *71*, 239-265.

(108) Dietze, D. R.; Mathies, R. A. Femtosecond Stimulated Raman Spectroscopy. *ChemPhysChem* **2016**, *17*, 1224–1251.

(109) Padalkar, V. S.; Tsutsui, Y.; Sakurai, T.; Sakamaki, D.; Tohnai, N.; Kato, K.; Takata, M.; Akutagawa, T.; Sakai, K.-i.; Seki, S. Optical and Structural Properties of ESIPT Inspired HBT–Fluorene Molecular Aggregates and Liquid Crystals. *J. Phys. Chem. B* **2017**, *121*, 10407-10416.

(110) Baranov, M. S.; Lukyanov, K. A.; Borissova, A. O.; Shamir, J.; Kosenkov, D.; Slipchenko, L. V.; Tolbert, L. M.; Yampolsky, I. V.; Solntsev, K. M. Conformationally Locked Chromophores as Models of Excited-State Proton Transfer in Fluorescent Proteins. *J. Am. Chem. Soc.* **2012**, *134*, 6025-6032.

(111) Chen, C.; Liu, W.; Baranov, M. S.; Baleeva, N. S.; Yampolsky, I. V.; Zhu, L.; Wang, Y.; Shamir, A.; Solntsev, K. M.; Fang, C. Unveiling Structural Motions of a Highly Fluorescent

Superphotoacid by Locking and Fluorinating the GFP Chromophore in Solution. *J. Phys. Chem. Lett.* **2017**, *8*, 5921–5928.

(112) Nogueira, B. A.; Castiglioni, C.; Fausto, R. Color Polymorphism in Organic Crystals. *Commun. Chem.* **2020**, *3*, 34.

TOC Graphic

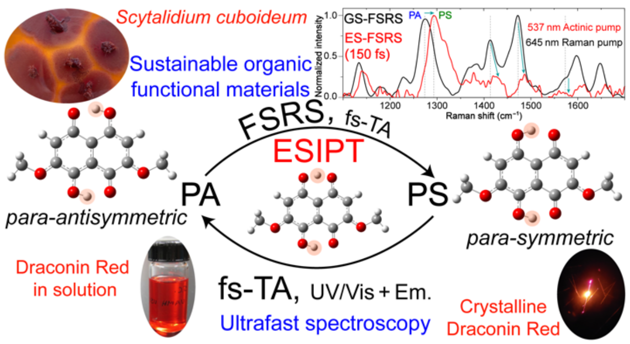
Scytalidium cuboideum
Sustainable organic functional materials
GS-FSRS
ES-FSRS (150 fs)
PA → PS
537 nm Actinic pump
645 nm Raman pump
Normalized intensity
1.0
0.5
0.0
1200
1300
1400
1500
1600
Raman shift (cm⁻¹)
FSRS, fs-TA
ESIPT
PA
PS
para-antisymmetric
para-symmetric
Draconin Red in solution
fs-TA, UV/Vis + Em.
Ultrafast spectroscopy
Crystalline Draconin Red